DATA-DRIVEN PREDICTION MODELING FOR PART ATTRIBUTES AND PROCESS MONITORING IN ADDITIVE MANUFACTURING

A thesis presented to the faculty of the Graduate School of Western Carolina University in partial fulfillment of the requirements for the degree of Master of Science in Engineering & Technology

By
Jayanta Bhusan Deb

Advisor: Dr. Nazmul Ahsan

Assistant Professor

School of Engineering and Technology

Committee Members:
Dr. Paul Yanik, School of Engineering and Technology
Dr. Basel Alsayyed Ahmad, School of Engineering and Technology

JUNE 2023

DECLARATION OF CO-AUTHORSHIP AND PREVIOUS PUBLICATIONS

Co-authorship

I confirm that my thesis includes content that is the result of my research, which was conducted under the guidance of Dr. Nazmul Ahsan. Dr. Ahsan is also a co-author of the papers produced in this research. While I was responsible for the primary contributions, including the study's novelty, data analysis, interpretation, and writing, Dr. Ahsan provided valuable feedback and comments and was an advisor.

Previous Publications

This thesis contains sections that are based on original papers previously submitted/published/will be published in peer-reviewed American Society of Mechanical Engineers (ASME) conferences. Please refer to the following table for details:

Publication Title	Publication Status	Inclusion in thesis
J. Deb, N. Ahsan, and S. Majumder, "Modeling the Interplay Between Process Parameters and Part Attributes in Additive Manufacturing Process with Artificial Neural Network," in IMECE2022, Volume 2A: Advanced Manufacturing, Oct. 2022. doi: 10.1115/IMECE2022-95120.	Published	Chapters 1-5
J. Deb, and N. Ahsan, "A Data-Driven Process Monitoring Approach for Time Series Machine Bed Vibration Prediction in Additive Manufacturing," in SMASIS 2023, Smart Materials, Adaptive Structures and Intelligence Systems, Sep. 2023. [Ref: SMASIS 2023-111142]	Under-review	Chapters 1-5

Self-Declarations

I confirm that the work described in this thesis was completed during my enrollment as a graduate student at Western Carolina University. My thesis does not violate any copyright or proprietary rights. Any material, such as ideas, quotations, or techniques, taken from other individuals' work has been appropriately acknowledged through standard referencing practices. This is an original copy of my thesis, including any final revisions that my thesis committee and the Graduate Studies office approved. Furthermore, I confirm that I have not submitted this thesis to any other University or Institution in pursuit of a higher degree.

DEDICATION

I am grateful to Western Carolina University for allowing me to contribute to advanced engineering and develop my scientific thinking. I am incredibly thankful to my advisor, Dr. Nazmul Ahsan, for his patient guidance throughout my research. In addition, I would like to thank my good friends, MD Shafiqul Alam, MD Sirajul Islam, MD Sadequr Rahman Bhuiyan, MD Saidur Rahman Roney, AJ Mongold, Lucas Lombard, William O'Shields, and Shilpa Chowdhury, for their knowledge and work experience. Lastly, I dedicate this thesis to my parents and two little sisters, who have continuously supported me in pursuing my dreams.

ACKNOWLEDGEMENTS

As a requirement for completing my Master of Science in Engineering and Technology degree at Western Carolina University, I conducted this research with the support of various laboratories, including the Maker Space, Machine Shop, and Materials Processing Laboratory. I want to acknowledge the invaluable help of these facilities, as well as the overall resources of the university, which made this research possible. Additionally, I am deeply grateful for the patience and guidance of my advisor, Dr. Nazmul Ahsan, particularly during the early stages of my research work when I had limited knowledge in this field. Under his mentorship, I gained much knowledge, and I express my sincere appreciation to him.

I want to express my gratitude to Dr. Paul Yanik and Dr. Basel Alsayyed Ahmad as they generously devoted their time to reviewing my thesis and providing feedback to enhance my research work's quality.

I want to extend my appreciation to Dr. Martin Tanaka for teaching me how to effectively articulate my thesis while adhering to the standards set by Western Carolina University. Additionally, I am grateful to Mr. Jerry Denton and Graduate Coordinator Dr. Paul Yanik for their constant support and for promptly making experimental and simulation equipment available.

I am grateful for the financial support that Western Carolina University provided me through graduate and summer assistantships. This assistance was vital in completing my studies and supporting myself while studying in the USA.

TABLE OF CONTENTS

LIST OF FIGURES

LIST OF TABLES

LIST OF ABBREVIATIONS

EOL	Experimental Overall Length
POL	ANN Predicted Overall Length
EOW	Experimental Overall Width
POW	ANN Predicted Overall Width
EASR	Experimental Average Surface Roughness
PASR	ANN Predicted Average Surface Roughness
ENW	Experimental Narrow Width
PNW	ANN Predicted Narrow Width
ET	Experimental Thickness
PT	ANN Predicted Thickness
ETS	Experimental Tensile Strength
PTS	ANN Predicted Tensile Strength
AM	Additive manufacturing
FDM	Fused deposition modeling
FFF	Fused filament fabrication
ANN	Artificial neural network
LSTM	Long short-term memory
VLSTM	Vanilla long short-term memory
RMSE	Root means square error
MSE	Mean square error
R	Correlation coefficient
EAV	Experimental Angular Velocity
PAV	Predicted Angular Velocity

ABSTRACT

DATA-DRIVEN PREDICTION MODELING FOR PART ATTRIBUTES AND PROCESS MONITORING IN ADDITIVE MANUFACTURING

Jayanta Bhusan Deb, MSET

Western Carolina University (June 2023)

Advisor: Dr. Nazmul Ahsan

The first study aimed to use artificial neural networks (ANN) to predict how process parameters would affect the part attributes in an extrusion-based additive manufacturing (AM) process. The study involved parts fabrication using an orthogonal array experimental design with five process parameters at three levels: building orientation, print speed, extrusion temperature, deposition direction, and layer thickness. The fabricated parts were measured for dimensional accuracy, surface roughness, and tensile strength. These attributes were then used to train, validate, and test multilayer ANN models. Three of the four ANN models were for predicting each of the three-part qualities separately, while the fourth was for combining all three attributes. Regarding RMSE and correlation coefficient, the findings showed that the individual part attribute ANN models outperformed the model for combining three attributes. To determine which parameters had a higher impact on the individual part qualities, comparisons between the individual part attributes with respect to the process parameters were made. The trained ANN models can forecast and optimize the part properties in extrusion-based AM processes. The second research developed a new method of collecting time series data for process monitoring in a Fused Filament Fabrication (FFF) system using wireless sensors to predict the machine bed angular velocity of FFF using the Vanilla Long Short-Term Memory (VLSTM) network. With two levels, the printer speed and deposition direction of the nozzle head were used in this study

following a full factorial experimental design to investigate their effects on machine vibration during printing. Time series machine bed angular velocity data were collected and used to train and test the proposed VLSTM network. Adam optimizer and VLSTM networks with four cells generated the best training accuracy after 100 epochs. One developed VLSTM model was used to train and test the network by inserting four-time series machine bed angular velocity data. Then four-time series simulation results were investigated to analyze the outputs of our developed and trained model. Simulation and experimental results were analyzed using root mean square error (RMSE). Practical data analysis concluded that the deposition direction of the nozzle head and printer speed both significantly affected the angular velocity of the printer bed. The developed VLSTM model can be used to predict the FFF printer bed angular velocity having different unexplored printer speeds and deposition directions, which will eventually help predict the quality of the printed parts through machine vibration analysis.

CHAPTER 1. INTRODUCTION

1.1 Introduction

Additive manufacturing, also known as 3D printing, is quickly overtaking other traditional production technologies in the manufacturing sector because of its ambitious tactics and desire to meet consumer demands and keep up with the current digitization of the manufacturing business. Compared to traditional manufacturing, which completes the building of the final goods using multiple steps with more tooling and significant amount of time, additive manufacturing completes the construction of the final products in one step with less tooling and time and in a more straightforward method [1]. Vat photopolymerization, material jetting, binder jetting, material extrusion, powder bed fusion, sheet lamination, and directed energy deposition are the different types of additive manufacturing technologies. Layer thickness, printing speed, nozzle temperature/laser power, infill percentage, infill pattern, build orientation, and deposition direction are important process variables for all additive manufacturing techniques where various materials are used for printing, and each method has its measurement for diagnosing system accuracy. Additionally, each technique has a final user application [2].

Extrusion-based 3D printing uses a heated moving nozzle to deposit particular materials layer by layer along a preset route or pattern [3]. Extrusion-based fused filament fabrication (FFF), also known as fused deposition modeling (FDM), techniques are more user-friendly and well-liked than other additive manufacturing processes for producing functional parts and finished products, as well as prototypes for product development and testing. This is because they are accessible, affordable, simple to use and maintain, and materials are readily available. To complete the overall fabrication, FDM employs polylactic acid (PLA), polyetherimide,

acrylonitrile butadiene styrene (ABS), polyether ether ketone, polycarbonate (PC), fiber-reinforced thermoplastic filament, etc., through a hot nozzle for the manufacture of parts [4].

The use of FDM technology is increasing in industrial sectors and medical sciences because of its more accessible post-processing techniques, material availability, and lower cost. However, the final quality of the printed parts can be affected by various process parameters and different manufacturing conditions [5], [6]. Advanced quality analysis and optimizing the process parameters are essential for the AM final printed products [7], [8]. Traditional optimization techniques require printing multiple samples and testing their performance, increasing the design process's time, effort, and cost. Furthermore, uncertainty and variations in process conditions/parameters and materials during printing may lead to defects and variability in parts [9], [10]. Therefore, reliable quality analysis and process monitoring systems are necessary to interpret the correlation between process parameters and process results in the FDM process to generate a better outcome.

1.2 Literature Review

The process parameters affect the mechanical qualities and printing quality. When employing FDM, users frequently need help getting the appropriate mechanical performance of the printed specimen. The threshold of each process parameter more strongly influences the ultimate quality of the built pieces. The tensile strength of materials is greatly influenced by nozzle temperature and layer thickness; tensile strength rises as nozzle temperature increases, and the reverse phenomenon occurs as nozzle temperature falls. Similarly to this, decreasing layer height can lead to an increase in tensile strength, while increasing layer thickness can have the opposite effect [11]. Surface quality is improved by reducing layer thickness [12]. Due to the lack of bonding time between deposited filaments, the material’s tensile strength decreases as the

raster angle or the angle between deposition direction and loading direction grows, and the printing speed climbs [2]. The essential process factors for the build part's quality in terms of surface roughness are the layer thickness, build orientation angle, and infill deposition angle. The material’s ultimate tensile strength and elastic modulus are significantly influenced by layer thickness, infill percentage, top/bottom layers, solid shells, and build orientation [13]. Regarding dimensional accuracy, Mohamed et al. [11] showed that diameter error increased with a decrease in deposition angle, but the error decreased with an increase in slice thickness. Length error fell after lowering the slice thickness, deposition angle, and part print direction. Previous research has found that the key to producing high-quality goods is to combine the input process parameters in the best possible way.

Changing various FDM process parameters is crucial to enhancing the final part's strength, surface quality, and accuracy [14]. A user needs help realistically executing a series of test prints and extensive experimentation to identify the ideal levels of the process parameters providing the required component quality. Due to the necessity of this considerable testing, the mechanical attributes of the FDM-fabricated item are also variable and sometimes overlooked. The process influences on surface quality and dimension accuracy are also significant. Therefore, the fabrication process uncertainties restrict FDM components’ use in industrial and mission-critical settings.

The experimental labor required to estimate certain part qualities can be reduced using computational geometry-based techniques. For example, in earlier research [15], [16], computational geometry-based methods were used to analyze the 3D geometric model of components to identify the best values for process parameters such as building orientation and deposition direction to maximize surface quality and manufacturability. However, these

approaches theoretically estimate the part properties. Additionally, these methods are not designed to predict the mechanical characteristics of 3D-printed objects.

To forecast the characteristics of 3D printed objects, machine learning techniques have recently been applied in additive [17] and advanced [18] manufacturing. The most popular machine learning technique for prediction and classification is the artificial neural network (ANN) [19]. To increase the component surface quality during the FDM process, the input parameters have recently been optimized using ANN due to their effectiveness in pattern recognition [20]. To anticipate the top and bottom surface quality of FDM items printed using PLA material, Kandananond et al. [21] employed an ANN model and the Box Behnken technique to optimize process parameters such as bed temperature, print speed, and layer thickness. However, while modeling the parameters-attributes connection using ANN, the prior studies have mainly concentrated on each attribute rather than considering the primary component attributes in a holistic approach. Due to the complicated dynamics and uncertainties in the FDM process, the model's holistic aspect must be considered.

It is found in the literature related to the process monitoring in FDM that infrared (IR) imaging cameras, thermocouples, pyrometers, vibration meters, optical emission spectrometers, and displacement sensors were used to measure temperature, vibration, optical emissions, and strain to analyze process conditions and detect defects in parts [22]–[25]. An online monitoring technique was developed by Rao et al. [26], which used thermocouples, accelerometers, and infrared temperature sensors to detect the failures in the desktop 3D printer by applying advanced Bayesian non-parametric analysis. Humidity, airflow, and temperature also impact the quality of the final printed parts. These environmental factors could affect internal geometry, mechanical strength, and surface quality [5]. Menderes et al. [27] investigated the effect of 3D

printer system vibrations on the mechanical properties of the printed parts. Some researchers used some other techniques [28]–[30]. So, monitoring machine vibration (acceleration, angular velocity, etc.) is vital to detect faults in manufactured parts to eliminate defects/scraps and maintain high standards for part quality. Additionally, the angular velocity of the printer bed is another factor that can impact the printing quality of the printed parts. Therefore, it is essential to investigate the effects of FDM process parameters on the printer angular velocity and predict it to maintain good printing quality.

1.3 Contribution of the First Study

The first study used artificial neural networks (ANN) to simulate the interaction between the process parameters and three fundamental component properties. This work produced components with three levels using an orthogonal array experimental design having five process parameters, including build orientation, print speed, extrusion temperature, deposition direction, and layer thickness. The developed artificial neural network models are trained, validated, and tested using measurements of three properties of the manufactured components, including dimensional correctness, surface roughness, and tensile strength. A comprehensive ANN model combined all three-part qualities and three distinct ANN models developed for each attribute. To determine which process factors, impact the individual component qualities, comparisons between the individual part attributes regarding those parameters were made. The user may improve the process parameters and component characteristics without investing in expensive and time-consuming fabrication trials by using the trained ANN models to forecast the following attributes of various parts for different undiscovered process parameter levels.

1.4 Contribution of the Second Study

The second study utilized a novel wireless sensor-based approach to collect time series angular velocity data, aiming to investigate the influence of deposition directions and printing speeds on the angular velocity of FDM printers and develop a time series angular velocity prediction model. Two levels of printer speed and deposition direction with a full factorial design of the experiment were chosen to examine their impact on the angular velocity of the printer bed. Additionally, a Vanilla Long-Short-Term Memory (VLSTM) model was developed to forecast the angular velocity of the printer bed for the forthcoming layers using the time series angular velocity data of the initial four layers. The model was trained extensively to optimize its performance before testing. Furthermore, time series test results were investigated for full factorial design combinations of printer speeds and deposition directions. The VLSTM model developed in this study can estimate the angular velocity of future layers for different unexplored printer speeds and deposition directions based on prior printing layer data. The estimated angular velocity for future layers can be used to analyze and detect potential anomalies ensuing in the printing process and take decisions on corrective actions.

CHAPTER 2. BACKGROUND

2.1 Extrusion-Based Fused Deposition Modeling

With extrusion-based 3D printing, the desired item is created by layer-by-layer deposition of specified materials using a moving nozzle under the guidance of G code from the printing machine software. Extrusion-based fused filament fabrication is distinct from other techniques due to its simplicity, accessibility, affordability, usability, maintainability, and the availability of materials and prototypes for product development and testing.

Weake et al. [1] used fused deposition modeling to forecast the tensile strength of materials based on polylactic acid (PLA). The process parameters of a twin extruder 3D printer were optimized using this model, which was also employed by Teharia et al. [2]. The Fused Filament Fabrication System's process variables were optimized using tensile specimens made of PLA [31]. Tura et al. [19] conducted an experimental analysis using fused deposition modeling to enhance the items' quality. To improve the fused filament fabrication process parameters and boost material strength, Pazhamannil et al. [4] conducted research. Fused deposition modeling is used to forecast and simulate the dimensional accuracy of components made using FDM [11]. Fuzzy logic was employed by Femi-Oyetoro [3] in fused deposition modeling to improve dimensional accuracy.

2.2 Artificial Neural Network

Artificial intelligence has been used in the past few years to optimize the process parameters for attaining the preferred product consumer's desire. The application of artificial intelligence for solving complex problems such as computing, physical sciences, engineering,

and statistics is increasing daily. Supervised, Unsupervised, and Reinforced machine learning are different techniques for solving complex problems. Neural Network is an example of supervised machine learning, which can recognize patterns after judging the nonlinear relationships between the input and output factors.

The artificial neural network is a popular machine learning tool for forecasting and prediction that functions similarly to the neurons in the human brain in terms of learning, adapting, and changing. In this method, each input neuron has an activation function that processes the weighted sum of each input to produce output. An additional bias input changes the net input to the activation function. The hidden layer's hidden neurons significantly impact how the network is designed and connected from the input signal to the output signal. Feed-forwarding networks are frequently used when training an ANN model with input data. The error backpropagation method uses hidden neurons in the hidden layer to identify the best pattern after calculating the correlation coefficient between the self-sufficient input variables and relying on output variables [19].

Weake et al. [1] applied an artificial neural network using nozzle temperature, layer thickness, and infill speed as input parameters and one hidden layer with ten neurons to predict output as tensile strength. Layer thickness, air gap, raster angle, build orientation, raster width, and the number of contours used as input in the ANN model, whereas the outputs are tensile strength, build time, and surface roughness [2]. Giri et al. [31] predicted the ultimate tensile strength of the ASTM standard specimen by applying an artificial neural network having layer thickness, nozzle temperature, speed rate, infill pattern, and raster orientation as process parameters. Tura et al. [19] used an artificial neural network model to determine the part quality of fabricated parts where layer thickness, orientation angle, and infill angle played a vital role.

Pazhamannil et al. [4] improved the engineering stress by applying the ANN model and figured out the impact of layer thickness, orientation, and temperature on the stress of materials. Dimensional accuracy increased for FDM printed parts after applying an artificial neural network where slice thickness, raster-to-raster air gap, deposition angle, part print direction, bead width, and the number of perimeters were analyzed as process parameters [11].

2.3 Vanilla Long Short-Term Memory (VLSTM) Network

The issue of the gradients getting very small (i.e., vanishing gradient) during backpropagation across time in recurrent neural networks (RNNs) makes it difficult or impossible for the network to learn long-term dependencies. To overcome this vanishing gradient problem, Hochreiter and Schmidhuber [32] developed the LSTM method in 1997.VLSTM network is a long short-term memory (LSTM) network with one input layer, one hidden layer of LSTM units, and an output layer to make the prediction. LSTMs are different from traditional feed-forward neural networks because of their feedback connections. This characteristic helps LSTM process the entire sequence of time series data instead of treating every point individually. By following this, LSTM collects valuable information about previous data points in the sequence to predict future data sets. As a result, complex machine-learning problems have been solved using the LSTM model. Instead of neurons, LSTM networks with memory blocks are connected through the whole hidden layer. Memory blocks can update the information depending on the time series of sequential data. That is why memory blocks are used in LSTM rather than using neurons in the hidden layers [33]. An optimized machine learning model has been developed in this study for data-driven time series prediction of machine bed angular velocity.

The output of the LSTM network depends on the current cell state, the previous hidden state's output, and the present state's input data. A memory block of the LSTM network consists of three gates: forget gate, an input gate, and an output gate. The network topology in a memory block is shown in Figure 1. The input gate consists of an input gate and an input node (new memory network). The forget gate decides which pieces of the previous hidden state and new data point in the sequence have less or more weight. To do this, it receives the previous hidden state and new input data; then, this network generates a vector in the range from 0 to 1 using the sigmoid activation function. Finally, the network in the forget gate receives the information when it is closer to 1 and vanishes the irrelevant information closer to 0. The goal of the input gate is to add new information to the network's long-term memory. After combining the previous hidden state and new input data, the input node generates a new memory update vector network with the help of the tanh activation function, which contains the essential information. The input node is not capable of remembering new information. That is why the input gate is sigmoid activated, which works as a filter and makes the new memory update vector network worth retaining. So, the resulting information should be input gate regulated. After pointwise multiplication of the vectors generated from the input gate and input node (6), the resultant vector is added to the cell state (5) to update the long-term memory of the network (7). The output gate used updated cell state, previous hidden state, and new input data to generate new hidden state. The output gate stores the relevant information using a sigmoid-activated neural network. The output gate generates a filter vector from the previous hidden state and current input. Finally, pass the updated cell state to the $\tan h$ activation to force information to store between -1 to 1. Then the filter vector was applied to the updated cell state as a pointwise multiplication to generate a new hidden state as output (8).

$$f_t = \sigma[(w_{fh}h_{t-1}) + (w_{fx}h_{t-1}) + b_f \quad (1)$$

$$i_t = \sigma[(w_{ih}h_{t-1}) + (w_{ix}h_{t-1}) + b_i \quad (2)$$

$$g_t = \tan h\,[(w_{gh}h_{t-1}) + (w_{gx}h_{t-1}) + b_g \quad (3)$$

$$o_t = \sigma[(w_{oh}h_{t-1}) + (w_{ox}h_{t-1}) + b_o \quad (4)$$

$$C_t^f = f_t C_{t-1} \quad (5)$$

$$C_t^i = i_t g_t \quad (6)$$

$$C_t = C_t^i + C_t^f \quad (7)$$

$$h_t = \tan h\,(C_t) o_t \quad (8)$$

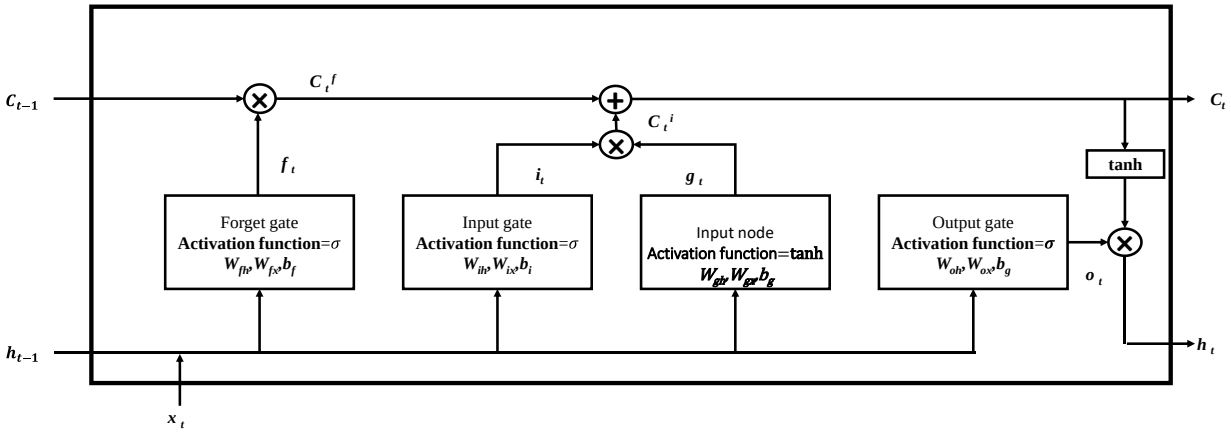

Figure 1: Memory block [34] of a LSTM cell

Every gate inside a memory block is controlled by a sigmoid activation network but the input node used the $\tan h$ activation unit. Each block receives the previous hidden state and current data as input sequences. The result of forget gate, input gate, input node, and output gate

are shown in (1)-(4) respectively. σ is a sigmoid and $\tan h$ is a tan activation function. $w_{fh}, w_{ih}, w_{gh} and\ w_{oh}$ are the weights for hidden state and $w_{fx}, w_{ix}, w_{gx} and\ w_{ox}$ are the weights for input of the respective gates, h_{t-1} is the output at time step (t – 1) of the previous hidden state of LSTM block, $b_f, b_i, b_g and\ b_o$ are biases for the respective gates and input is denoted by x_t at the current time step.

2.4 Taguchi and Full Factorial Array Design of Experiment

Any researcher can move for preliminary testing before beginning a massive experiment by using a unique type of experiment design called a Taguchi Orthogonal Array. Thus, using Taguchi Orthogonal Array, the experimental cost can be easily reduced. Various Taguchi orthogonal array types have been adopted by multiple scholars recently. Due to the employment of the Taguchi L9 orthogonal array by Weake, Tura, and Pazhamannil [1], [4], [19], respectively, who had three different process parameters with three different levels, the entire experimental run was reduced from 27 to 9. Weake et al. [1] employed a Taguchi L9 orthogonal array to design an experiment to anticipate the ultimate tensile stress of the ABS material by optimizing process parameters such as layer thickness, building orientation, and printing temperature. For design, they used ASTM D-638 tensile standard specimens. Teharia et al. [2] employed the L27 Taguchi Orthogonal Array as a design experiment with six different process parameters to cut the expense and duration of the investigation. L27 orthogonal array was utilized by Femi-Oyetoro et al. [3] to reduce the experimental data. A full factorial array design of experiment utilized based on extruder temperature, material flow rate and printing speed for monitoring temperature and vibration data in FDM process [35].

2.5 Instron Tensile Testing Machine

Weake et al. [1] tested the tensile strength of polylactic materials in fused deposition modeling by breaking nine experimental prototypes with a SHIMADZU-AGX 10KN universal testing equipment. Giri et al. [31] broke 27 samples using the computerized tensile testing machine 50KN to forecast the tensile strength using ANN. Pazhamannil et al. [4] used an electromechanical universal tensile testing machine to estimate the tensile strength of ABS material.

2.6 SPI Surface Roughness Tester

Teharia et al. [2] measured the surface roughness of 21 samples using the roughness test to estimate the surface roughness using ANN. Laser scanning microscopy (VK-X 200 K, Keyence, Japan) was used by Tura et al. [19] to assess the surface roughness of nine experimental trials.

2.7 3D printing machine

Before beginning the tensile test, Weake et al. [1] used an Aha 3D printer to manufacture all of their specimens. Twenty-seven prototype parts were printed on a Fusebot 250 printer [31]. The Ultimaker Cura software utilized FDM Flash forge creator pro, which is used by Tura et al. [19]. Pazhamannil et al. [4] printed the specimens on a Cube Pro dual printer.

2.8 Dimension Measuring Machine

Digital calipers were primarily used in earlier research to measure the printed specimens' dimensions [36], [37].

2.9 Design and Coding Software

PTC Creo was used by Mohamed et al. [11] to create the ASTM standard sample. Software such as Solid Works [38] and AutoCAD [39] was utilized by certain studies to design their specimen. The most popular coding languages for creating neural network models for training, validating, and testing data are MATLAB [40] and Python [41].

2.10 Design of Experiment Software

The Taguchi L27 orthogonal array was used to design the experiment using Minitab. Weake et al. [1] used the L9 Taguchi Orthogonal Array in Minitab software to shorten their trial run. Minitab 18 was utilized by Pazhamannil et al. [4] to calculate the experiment run from L27 to L9, while Minitab V19 was used by Giri et al. [31] to design the L27 orthogonal array.

3.METHODOLOGY

3.1 Methodology for ANN Based Prediction Modeling

3.1.1 Design of Specimen

This study used the standard test method for the tensile characteristics of plastics, and the ASTM D638-14 Type I specimen design, as illustrated in Figure 2. Prior FDM research has also utilized standard specimens, such as ASTM D638-14 standard dog bones [2], [4], [19], to preserve consistency in the printing and measuring processes. The tensile qualities of plastics were examined on the Type I specimens that were 3D printed using a standard procedure.

3.1.2 Material and printer

The specimens in this study were 3D printed using PLA material because it is a popular and environmentally friendly 3D printing medium. The standard samples were printed using a Prusa i3 MK-3 3D printer. The following section's process parameter levels were chosen based on the PLA material's material characteristics.

3.1.3 Selection of Process Parameter

Five process parameters were chosen following the FDM process configuration: layer thickness (LT), nozzle/extruder temperature (ET), printing speed (PS), build orientation (BO), and deposition direction. (DD). Three alternative degrees of each processing parameter were chosen based on the characteristics of PLA. The minimum layer thickness was chosen based on the machine’s resolution. The nozzle diameter was used to determine the upper limit of layer thickness.

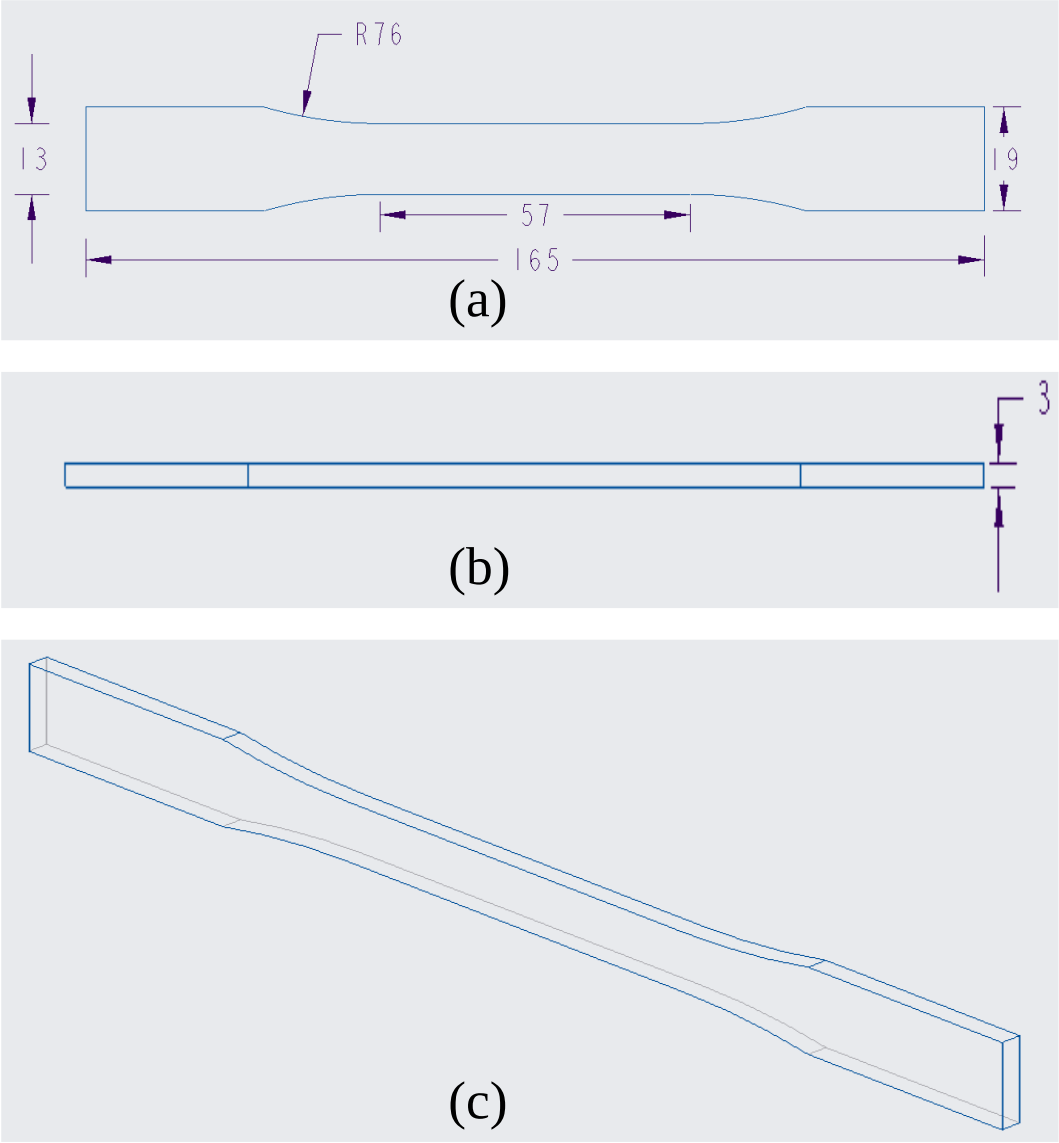

Figure 2 : Dimensions of the specimen include (a) Top View, (b) Front View, and (c) 3D View.

To examine the impact of the layer thickness on the part attributes throughout a range of 0.1 mm, three levels of the layer thickness—0.1 mm, 0.2 mm, and 0.3 mm—were chosen. The extruder temperatures were selected at 200°C, 210°C, and 220°C with an interval of 10°C for our studies because the printing temperature of PLA material spans from 180°C to 230°C. The Prusa 3D printer's printing capabilities led to the selection of printing speeds of 40 mm/s, 60 mm/s, and

80 mm/s while retaining a 20 mm/s spacing. Productivity increases when printing speeds improve since it takes less time to create a part. The machine's capabilities set a limit on the maximum print speed, and going faster could lead to poorer material deposition.

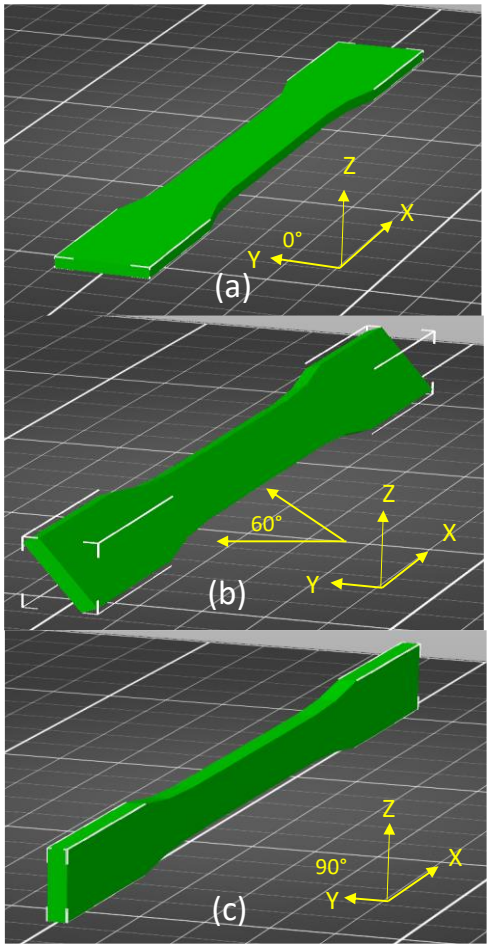

Figure 3 : Build orientations for experimental designs at 0°, 60°, and 90°

The build orientations of 0°, 60°, and 90° about the X-axis were selected as indicated in Figure 3 to cover the entire build orientation range about one orthogonal axis in the standard coordinate system. For every 3D printed specimen, a zigzag infill structure with 50% relative density was applied. The zigzag infill structure's deposition direction was chosen at 0°, 30°, and 45° (about along the Z-axis) to examine the impact of various infill angles on part properties.

The 0°, 30° and 45° deposition directions are followed, in turn, by 90°, 120°, and 135°, in the subsequent layers, as illustrated in Figure 4. Using PrusaSlicer Version 2.4.0, the sample 3D model was cut into slices while using all the selected process settings. Table 1 lists the process parameters and the chosen levels for each. While 0° and 90° build-oriented specimens were not given any support structure, 60° build-oriented samples were printed with it.

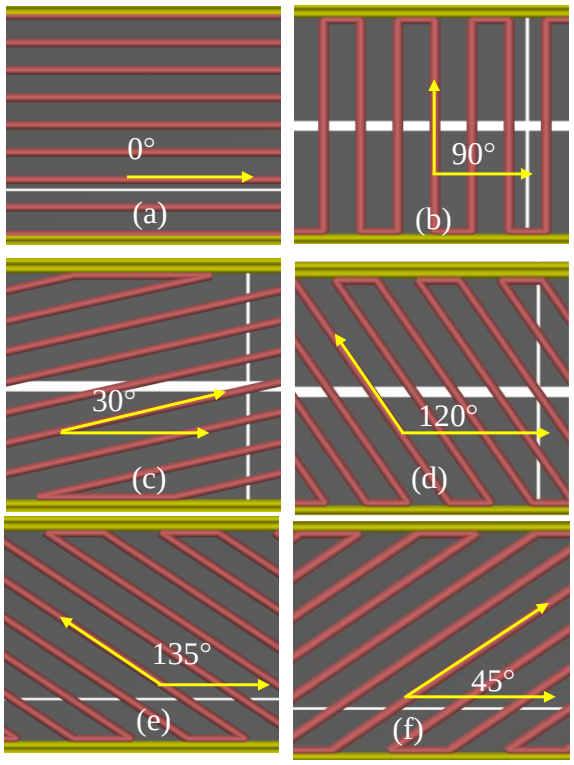

Figure 4 : Zigzag infill structure: (a) 0°, (b) 90°, (c) 30°, (d) 120°, (e) 45°, and (f) 135° deposition directions

Table 1 : Parameters of the process and their levels

Parameter	Unit	Level
Layer Thickness	mm	0.1/0.2/0.3
Extruder Temperature	°C	200/210/220
Printing Speed	mm/s	40/60/80
Build Orientation	Degree (°)	0/60/90
Deposition Direction	Degree (°)	0/30/45

3.1.4 Experimental Design

As a result of its excellent method for minimizing experimentation and choosing a unique combination of process parameters while considering no correlation among all the factors, the Taguchi Orthogonal Array was utilized as the design of the experiment. The Taguchi L27 Orthogonal Array in Table 2 was produced using the Minitab Version 10.0.19044 software.

Table 2: Design of Experiment for Taguchi L27 Orthogonal Array

Specimen	Layer Thickness	Extruder Temperature	Printing Speed	Build Orientation	Deposition Direction
1	0.1	200	40	0	0
2	0.1	200	40	0	30
3	0.1	200	40	0	45
4	0.1	210	60	60	0
5	0.1	210	60	60	30
6	0.1	210	60	60	45
7	0.1	220	80	90	0
8	0.1	220	80	90	30
9	0.1	220	80	90	45
10	0.2	200	60	90	0
11	0.2	200	60	90	30
12	0.2	200	60	90	45
13	0.2	210	80	0	0
14	0.2	210	80	0	30
15	0.2	210	80	0	45
16	0.2	220	40	60	0
17	0.2	220	40	60	30
18	0.2	220	40	60	45
19	0.3	200	80	60	0
20	0.3	200	80	60	30
21	0.3	200	80	60	45
22	0.3	210	40	90	0
23	0.3	210	40	90	30
24	0.3	210	40	90	45
25	0.3	220	60	0	0
26	0.3	220	60	0	30
27	0.3	220	60	0	45

3.1.5 Experimental Setup

Twenty-seven specimens with two replicas each were printed using a Prusa i3 MK3 3D printer. After calibration, a digital micrometer caliper was used to precisely measure the key measurements of the 3D printed specimen pieces, including overall length (OL), overall width (OW), narrow width (NW), and thickness (T). As illustrated in Figure 5, the average surface roughness (SR) of printed parts was measured along both lateral and transverse directions using an SPI Portable Roughness Tester II with a 0.0002″ Stylus Tip Radius.

The ultimate tensile (TS) strength of the printed specimens was evaluated using the Instron 5967 tensile testing apparatus, depicted in Figure 6. This equipment's specimen fixture is pneumatically operated. 40 PSI pressure was employed to keep the specimens between the jaws to avoid any slippage in the grips. At a crosshead speed of 5 mm/min, tensile tests were run. Several examples are shown in Figure 7, both before and after tensile testing.

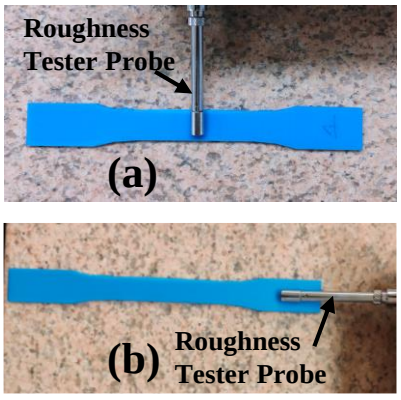

Figure 5 : Measurement of surface roughness in the specimen's (a) Lateral and (B) Transverse directions

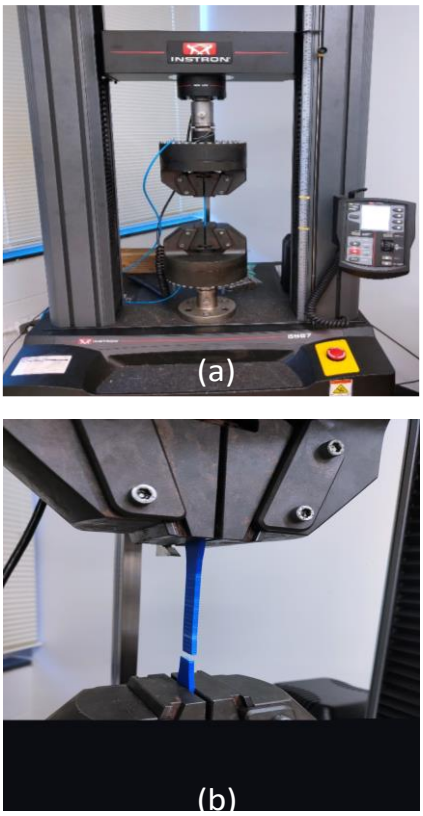

Figure 6 : Tensile Testing: (a) Loaded specimen and (b) Fractured specimen before and after testing.

(a) (b)

Figure 7 : Specimens prior to (a) and post (b) tensile testing

3.1.6 Artificial Neural Network Model

To train, test, and validate the ANN models, the process parameter combinations of the experimental design (Table 2) were used as the inputs, and the corresponding experimental data (strength, surface roughness, and dimensional accuracy) of the 3D printed specimens were used as the outputs. The ANN codes were implemented using MATLAB 2021a. The neural Pattern Recognition (NPR) toolbox was used to predict the data. After inserting the experimental data in the ANN network, data was normalized for better learning the neural network. Then train the ANN model to find the minimum error between training and validation dataset. After finding the lowest error between train and validation dataset, the model predicts the output attributes based on test datasets. Then the predicted value was denormalized for comparing with the actual data. Three separate ANN models were created to forecast the distinct part attributes—ultimate tensile strength, dimensional correctness, and surface roughness. A combined ANN model was also designed to depict the link between the three-part qualities and the five process parameters. 15% of the data were chosen for validation, 15% for testing, and 70% for training the ANN models at random. Specifically, specimens 4, 9, 11, and 25 were utilized for validation, while specimens 7, 16, 19, and 23 were used for testing. All additional samples were used for training. We identified the ideal number of hidden neurons after 70 iterations when the error between the training, validation, and test sets was as low as possible. Finally, the data were tested using the optimal number of neurons in the hidden layer [42].

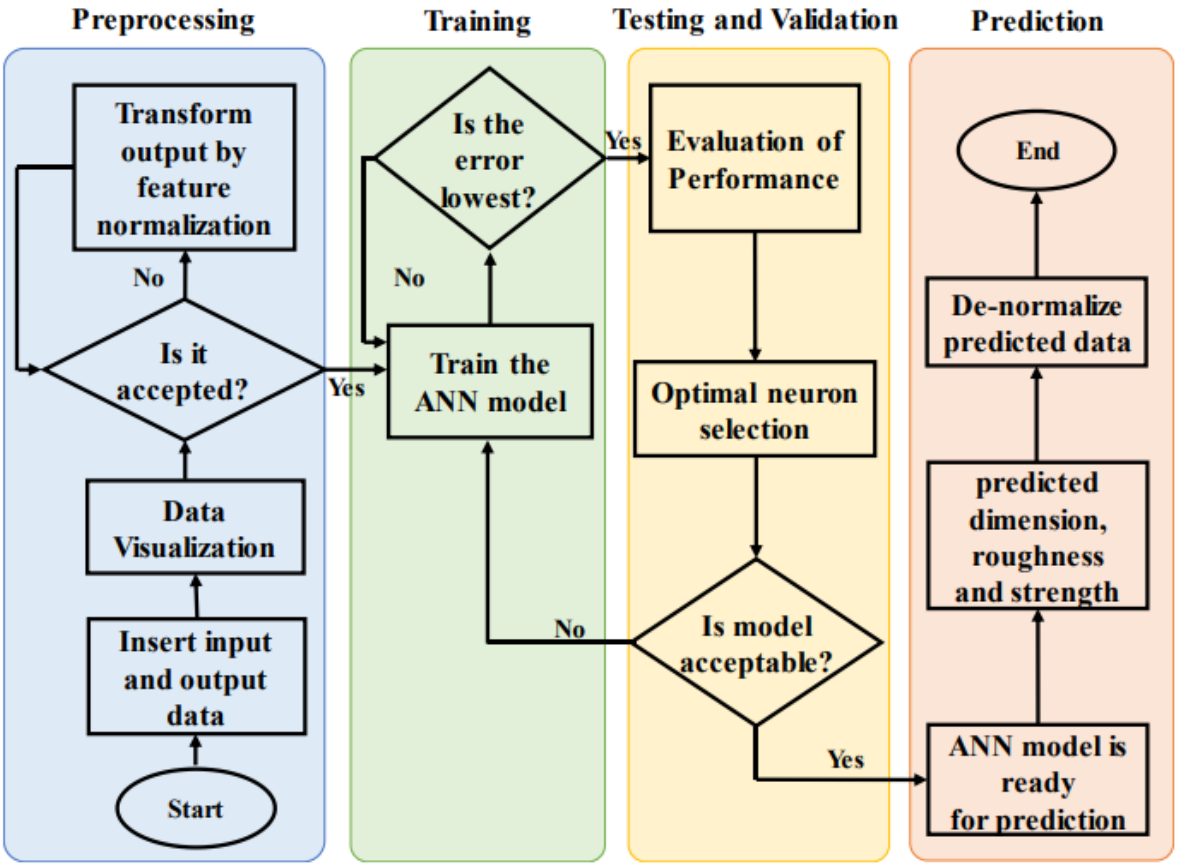

Figure 8 : Flow chart developed for ANN modeling.

The signal was transferred from the input layer to the output layer through the hidden layer using the tangent sigmoid function in the hidden layer and a purely linear function in the output layer (all outputs were normalized). The information is often transferred from one neuron layer to another in ANN models using sigmoid and linear functions [43]. The artificial neural network modeling procedure described in this paper's flow chart is shown in Figure 8, and the proposed framework is illustrated in Figure 9.

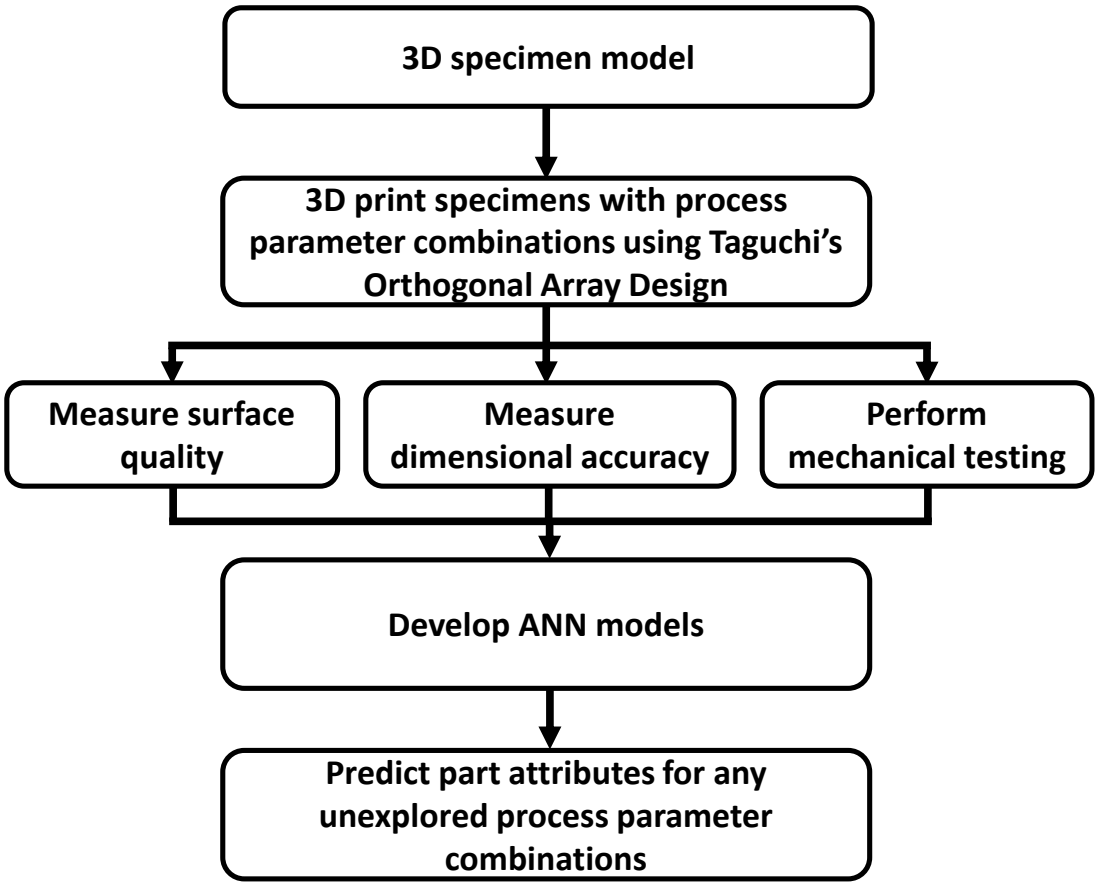

Figure 9: Proposed framework for ANN modeling

3.1.7 Loss Function and Correlation Coefficient Calculation

Mean square error (MSE) was used as a loss function in the developed ANN network. The MSE loss function is widely used as a loss function for regression analysis of the neural network. The average squared difference between the experimental and prediction data can be measured using the MSE loss function [44]. It can be expressed by using the following equation:

$$\text{Mean Square Error (MSE)} = \frac{1}{n} \sum_{j=1}^{n} (x_{ej} - x_{pj})^2 \qquad (9)$$

Here, n is the number of data points, x_{ej} is the value of experimental data and x_{pj} is the value of model predicted data.

The root means square error (RMSE) was used to determine the model's accuracy in both studies, which is the root of the mean square error [45]. The following equation can express it:

$$\text{Root Mean Square Error (RMSE)} = \sqrt{\frac{1}{n}\ \sum_{j=1}^{n}(x_{ej} - x_{pj})^2} \quad (10)$$

Here, n is the number of data points, x_{ej} is the value of experimental data and x_{pj} is the value of model predicted data.

To quantify the relationship between experimental and model predicted data correlation coefficient (R) was used [46]. It can be expressed by the following equation:

$$\text{Correlation Coefficient (R)} = \frac{\sum_{j=1}^{n}(x_{ej}-\overline{x_e})^2(x_{ej}-\overline{x_p})^2}{\sqrt{\sum_{j=1}^{n}(x_{ej}-\overline{x_e})^2 \sum_{j=1}^{n}(x_{pj}-\overline{x_p})^2}} \quad (11)$$

Here, n is the number of data points, x_{ej} is the value of experimental data and x_{pj} is the value of model predicted data, $\overline{x_e}$ is the value of average experimental data, and $\overline{x_p}$ is the value of average model predicted data.

3.2 Methodology for VLSTM Based Prediction Modeling

3.2.1 Specimen Design

In this study, ASTM D638-14 Type I standard was used to design the specimens (Figure 2) to ensure printing consistency [10]. A PRUSA i3 MK-3 3D printer was used to print the standard specimens because of its ease of use, reliability, and automatic bed leveling system. Polylactic acid (PLA) material was used to 3D print the specimens as it is a widely available and environmentally friendly material. PLA is well suited for a wide range of 3D printing

applications. Process parameter levels were selected depending on the characteristics of the PLA material and printer configuration as discussed in the following section.

Table 3: Process parameter setting for printed specimens.

Parameter	Value
Layer thickness	0.1 mm
Infill density	100%
Deposition direction	0°,45°
Printing speed	40 mm/s,80 mm/s
Nozzle temperature	220°C
Infill Pattern	Rectilinear
Build orientation	0°

3.2.2 Process Parameters Selection

Printing speeds (PS) and deposition directions (DD) were chosen after investigating the interaction plot (provided in section 4.2.2). It was found that printing speeds and deposition directions greatly influenced the printer bed vibration. Two levels of printing speeds, including 40 mm/s and 80 mm/s, were selected according to the printing capabilities of the Prusa 3D printing machine. Deposition directions were chosen as 0° and 45° (about Z-axis). Each of these angles was accompanied by another set of deposition directions at 90° and 135°, respectively, in a crisscross pattern for successive layers of the print, as shown in Figure 4. Printer speeds and deposition directions were chosen at their highest and lowest limits to differentiate their effect on printer bed vibration. The 3D printed specimens in this study were prototyped using rectilinear infill structures with 100% relative density. PrusaSlicer Version 2.4.0 was used for slicing the 3D model. The selected two levels of printing speeds, deposition directions, and all other constant process parameters are listed in Table 3. A full factorial design of the experiment was used to generate the combinations of deposition directions and printing speeds, as shown in Table 4.

Table 4: Full factorial array design of experiment.

Specimen	Printing Speed (mm/s)	Deposition Direction (°)
1	80	45
2	40	0
3	80	0
4	40	45

3.2.3 Experimental Procedure and Data Acquisition

This study investigated the impact of different printing speeds and deposition directions on machine vibrations while printing four dog bone prototype parts shown in Figure 11. Data was collected through a wireless vibration sensor (accelerometer-gyroscope), which recorded machine bed angular velocity data every second. To eliminate external vibration interference, the printing experiment was conducted on a Newport RS2000TM antivibration table. A high-performance laptop with a core i7 processor was used for real-time data collection. The wireless sensor was mounted underneath the printer bed, as shown in Figure 10. The average angular velocity for x, y, and z directions was calculated during the post-processing stage of the collected data and used for training and testing of our developed time series model. Specimen 1 was used to develop the VLSTM model, while Specimens 2, 3, and 4 were utilized to verify the model's accuracy.

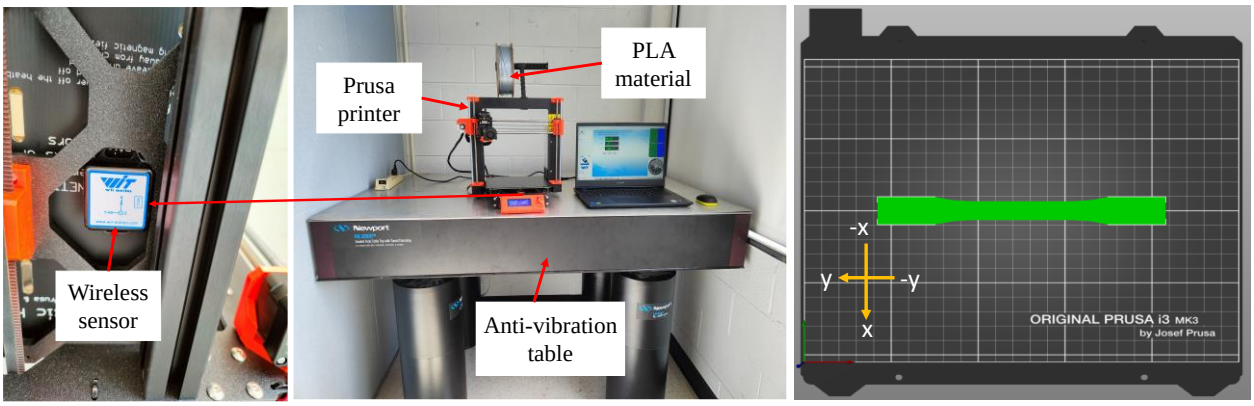

Figure 10: Data collection procedure

Figure 11: Printed specimens for the second study

3.2.4 VLSTM Model Selection Procedure

An optimized machine learning model has been developed for data-driven time series prediction of machine bed angular velocity. A special kind of recurrent neural network called vanilla long short-term memory (VLSTM) was selected for the process monitoring of FDM to overcome the long-term dependency problems of recurrent neural networks over time [47], [48]. The simulation was carried out on a laptop computer with an 11th Gen Intel(R) Core i7-11800H @ 2.30GHz processor having 16GB RAM. This research used the Python library Keras to develop the time series future angular velocity prediction model. The steps followed in selecting

the final VLSTM model are shown in Figure 12. The proposed framework described in Figure 13 and Figure 14 shows the experimental and simulation phase of VLSTM modeling.

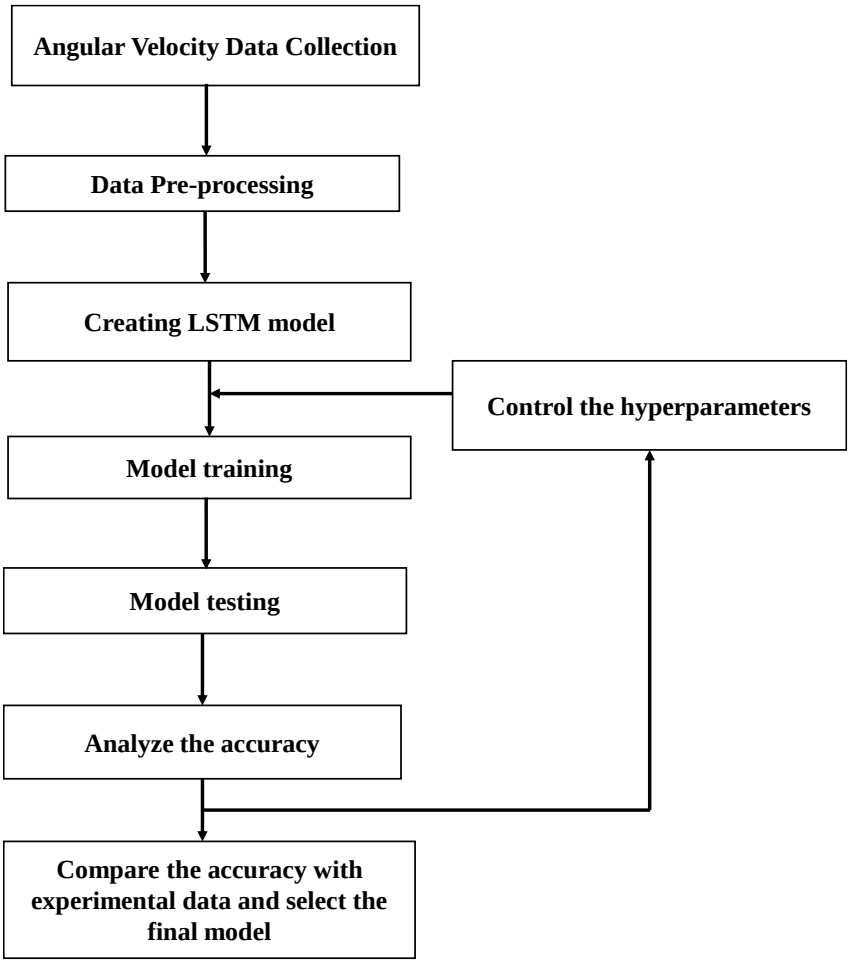

Figure 12 : Schematic for VLSTM modeling

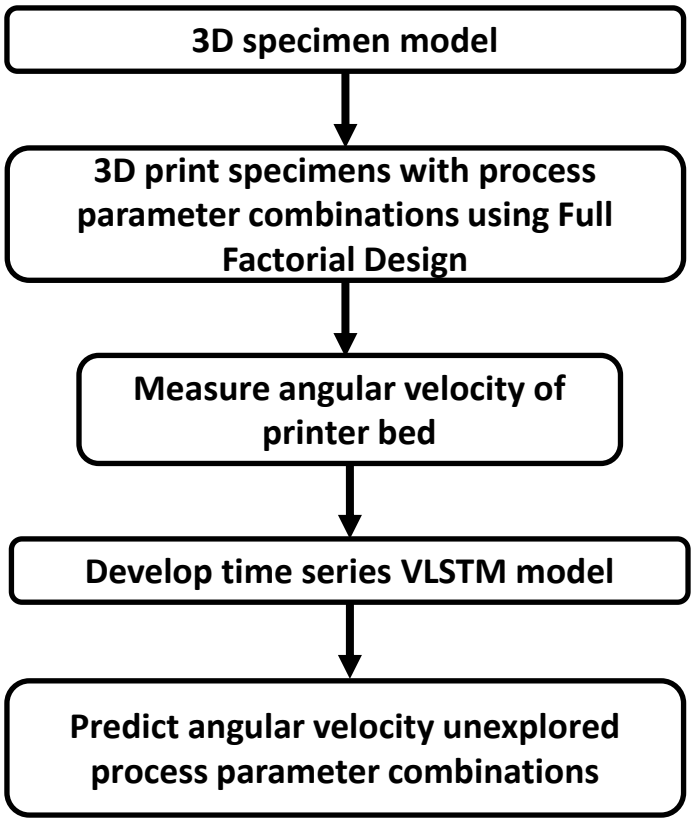

Figure 13 : Proposed framework for VLSTM modeling

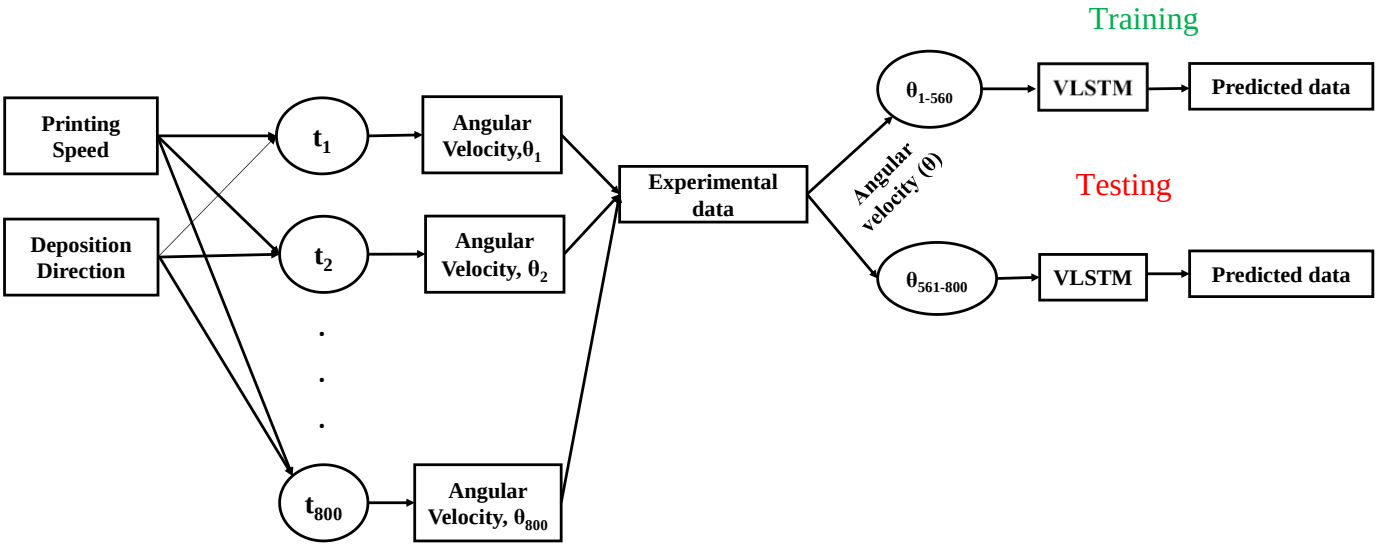

Figure 14 : Experimental and simulation phase in VLSTM modeling

3.2.5 Loss Function Calculation

Mean square error (MSE) was used as a loss function in the developed VLSTM network. The average squared difference between the experimental and prediction data can be measured using the MSE loss function [44]. It can be expressed by using the following equation:

$$\text{Mean Square Error (MSE)} = \frac{1}{m} \sum_{k=1}^{m} (y_{ek} - y_{pk})^2 \qquad (12)$$

Here, m is the number of data points, y_{ek} is the value of experimental data and y_{pk} is the value of model predicted data.

The root means square error (RMSE) was used to determine the model's accuracy in both studies, which is the root of the mean square error [45]. The following equation can express it:

$$\text{Root Mean Square Error (RMSE)} = \sqrt{\frac{1}{m} \sum_{k=1}^{m} (y_{ek} - y_{pk})^2} \qquad (13)$$

Here, m is the number of data points, y_{ek} is the value of experimental data and y_{pk} is the value of model predicted data.

CHAPTER 4. RESULTS & DISCUSSION

4.1 Results and Discussion for ANN modeling

4.1.1 Artificial Neural Network Model

To train the network and determine the ideal number of neurons in the hidden layer, a rule of thumb [42] was used. One hidden layer with six neurons and a tangent sigmoid transfer function performed the best for the combined output model after 70 epochs of training our generated artificial neural network models. A feed-forward neural network was used to determine the discrepancy between the experimental and predicted data. The weights were then adjusted via backpropagation, and the error was minimized by repeating the process. After examining several ANN network topologies, the ideal number of neurons in the hidden layer was discovered. Topological optimization with two and three hidden layers was also examined during the simulation phase. As shown in Table 5, the dimension accuracy prediction model, the surface roughness prediction model, and the tensile strength prediction model were all found to work best with the topological combinations 5-4-1, 5-9-4, and 5-7-1. Here, the input, hidden, and output layers' respective numbers of neurons are represented by the model topology's first, second, and third digits. Levenberg-Marquardt, Bayesian regularization, one-step secant, and gradient descent techniques were used to train the models where Levenberg-Marquardt performed better than the others.

Based on ANN model prediction data, root mean square error and correlation coefficient were determined to evaluate the model performance. The training data's decreased RMSE proved the artificial neural network's proper training. For all the models, the Pearson correlation

coefficient was close to one. Table 3 displays the RMSE findings for the four models and transfer function combinations. The optimized combined output model's ANN topology is shown in Figure 15. The three component qualities can be predicted using the combined output model, which should be very helpful for industrial businesses or a single user. The average surface roughness, tensile strength, and dimension accuracy forecasts in the combined ANN model performed almost equally well compared to the actual data, which increased the acceptance of the model, as shown in Figure 16. For all the datasets, including training, validation, and testing, the average root mean square error (RMSE) of the four distinct dimensions was determined to be 0.143289, the RMSE of the average surface roughness was 0.319013, and the RMSE of the tensile strength was 0.481639. The neural network regression plot analysis revealed that the model's gradient was at its lowest at epoch 5. When the least mean square error was determined among the training, validation, and testing data at epoch 5, the best validation performance was discovered to be 0.28312.

Table 5 **:** For the four models, optimized ANN topology with transfer function

Output prediction	**Topological combination**	**Transfer Function (hidden layer)**	**Transfer Function (output layer)**	**RMSE**
Dimensional Accuracy Model	5-9-4	tansig	purelin	0.140095
Surface Roughness Model	5-4-1	tansig	purelin	0.286078
Tensile Strength Model	5-7-1	tansig	purelin	0.421935
Combined Output Model	5-6-6	tansig	purelin	0.143289 (Dimension Accuracy) 0.319013 (Surface Roughness) 0.481639 (Tensile Strength)

The average root mean square error (RMSE) of four different dimensions for the individual model for dimensional accuracy was discovered to be 0.140095 for all the data points, including training, validation, and testing, which is more accurate than the combined prediction model. At epoch 4, the model has attained its gradient minimum. When the dataset's minimal mean square error was discovered at epoch 4, the best validation performance was determined to be 0.37542.

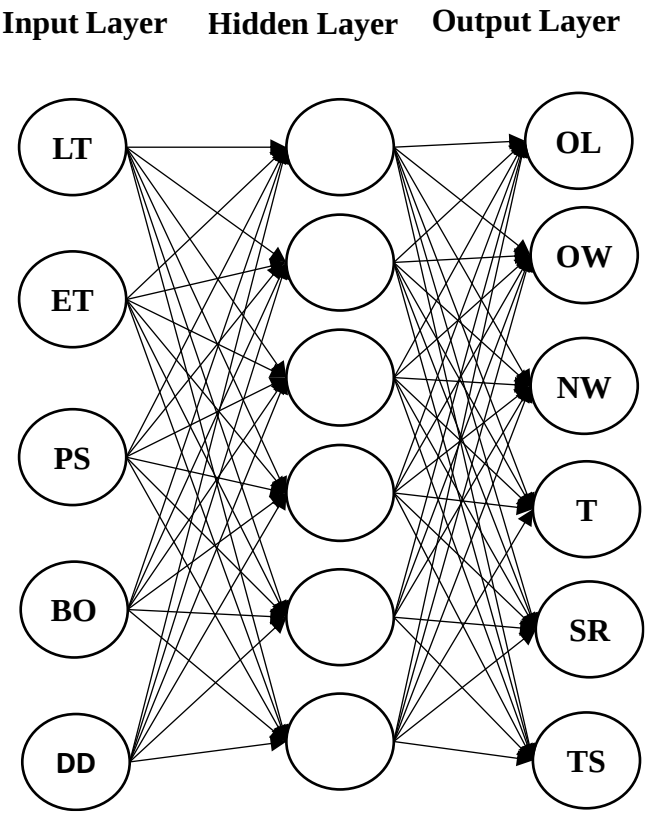

Figure 15 : ANN topology for optimized combined prediction model.

Figure 17 illustrates how well the experimental result and ANN projected average surface roughness findings agreed. It was discovered that the prediction error for the average surface

roughness using the individual model was lower than the forecast using the combined model. The average surface roughness model's root means square error (RMSE), less than the combined prediction model, was determined to be 0.286078 for all the data points, including training, validation, and testing. The study of the neural network regression plot revealed that epoch 4 was the model's minimal gradient. The least mean square error among training, validation, and testing data was determined to be 0.026448 at epoch 3 when the best validation performance was discovered.

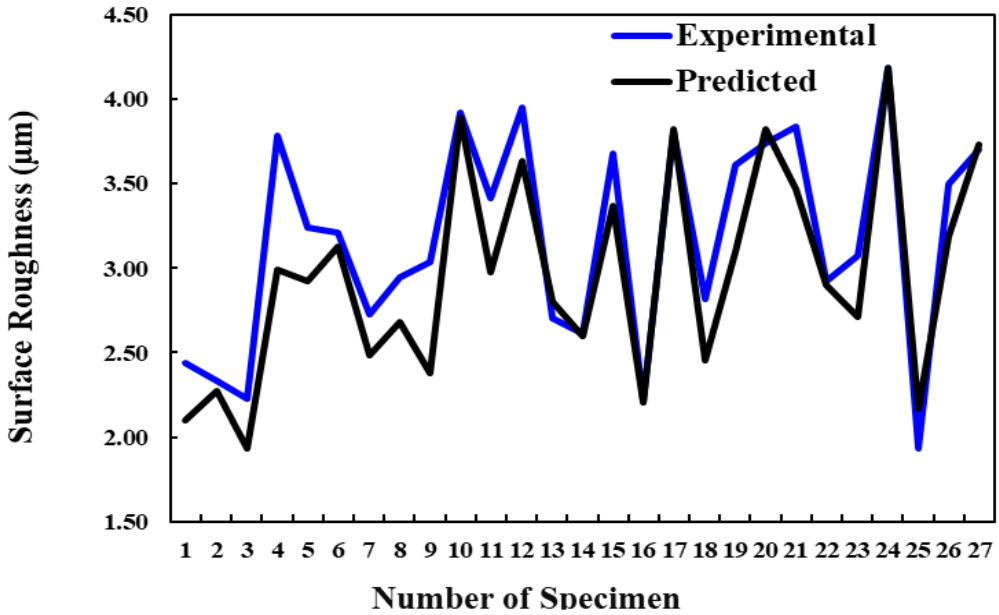

(a)

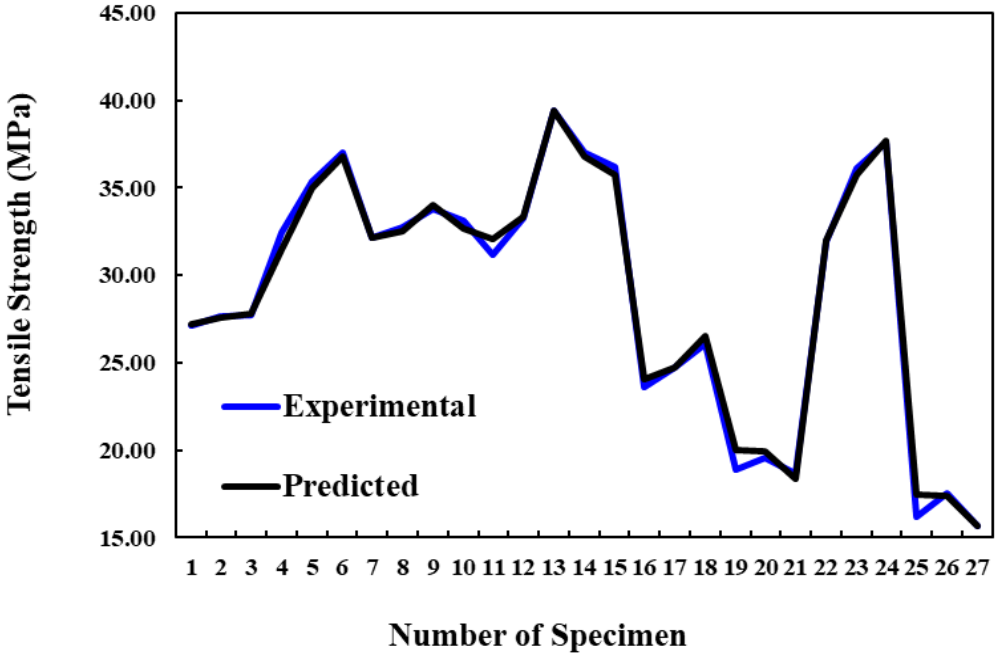
Tensile Strength (MPa)
45.00
40.00
35.00
30.00
25.00
20.00
15.00
Experimental
Predicted
1 2 3 4 5 6 7 8 9 10 11 12 13 14 15 16 17 18 19 20 21 22 23 24 25 26 27
Number of Specimen

(b)

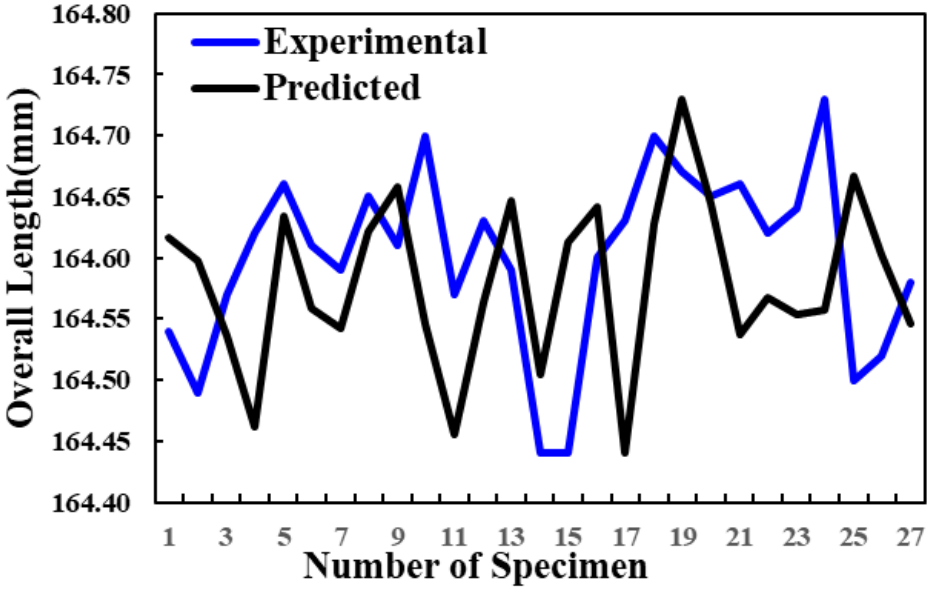
Overall Length(mm)
164.80
164.75
164.70
164.65
164.60
164.55
164.50
164.45
164.40
Experimental
Predicted
1 3 5 7 9 11 13 15 17 19 21 23 25 27
Number of Specimen

(c)

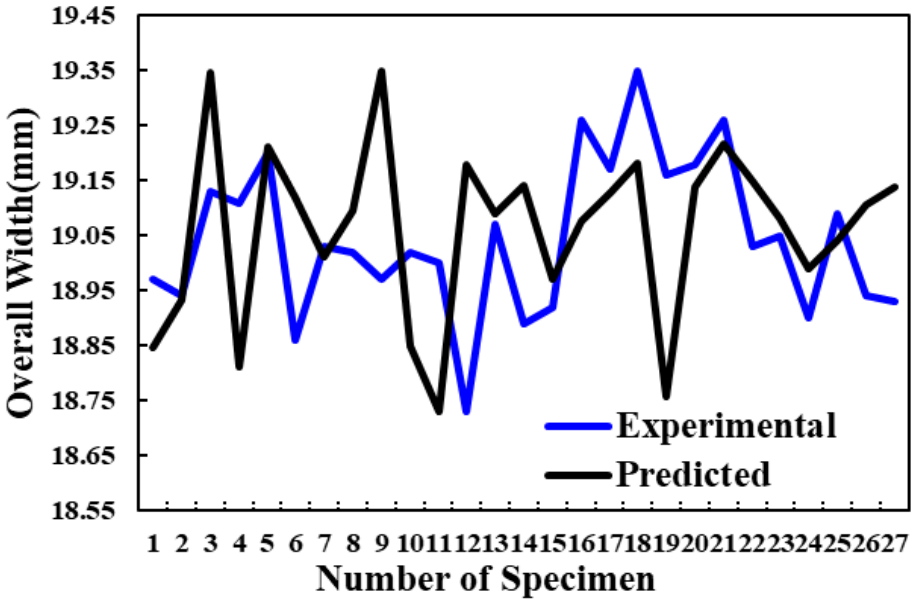
Overall Width(mm)
19.45
19.35
19.25
19.15
19.05
18.95
18.85
18.75
18.65
18.55
Experimental
Predicted
1 2 3 4 5 6 7 8 9 10 11 12 13 14 15 16 17 18 19 20 21 22 23 24 25 26 27
Number of Specimen

(d)

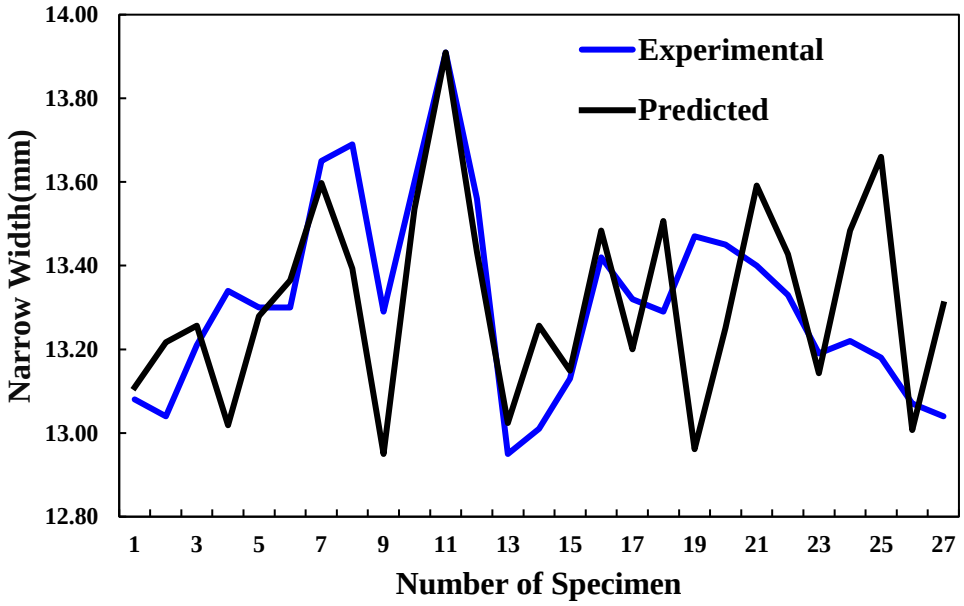
Narrow Width(mm)
14.00
13.80
13.60
13.40
13.20
13.00
12.80
Experimental
Predicted
1 3 5 7 9 11 13 15 17 19 21 23 25 27
Number of Specimen

(e)

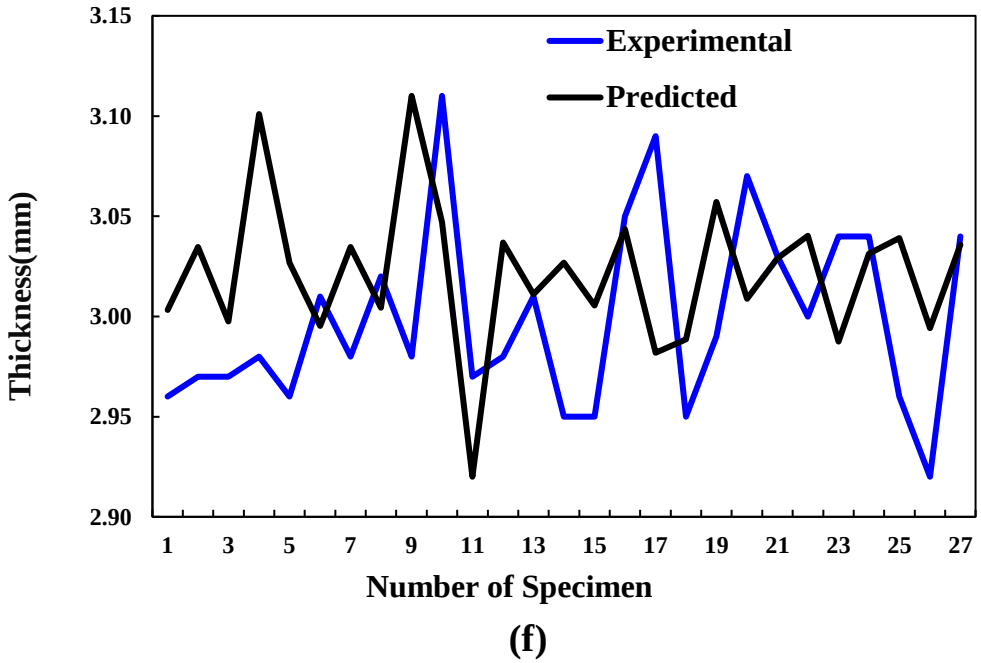

Figure 16 : Actual and predicted data for surface roughness (a), tensile strength (b), overall length (c), overall width (d), narrow width (e), and thickness (f) from the combined output model.

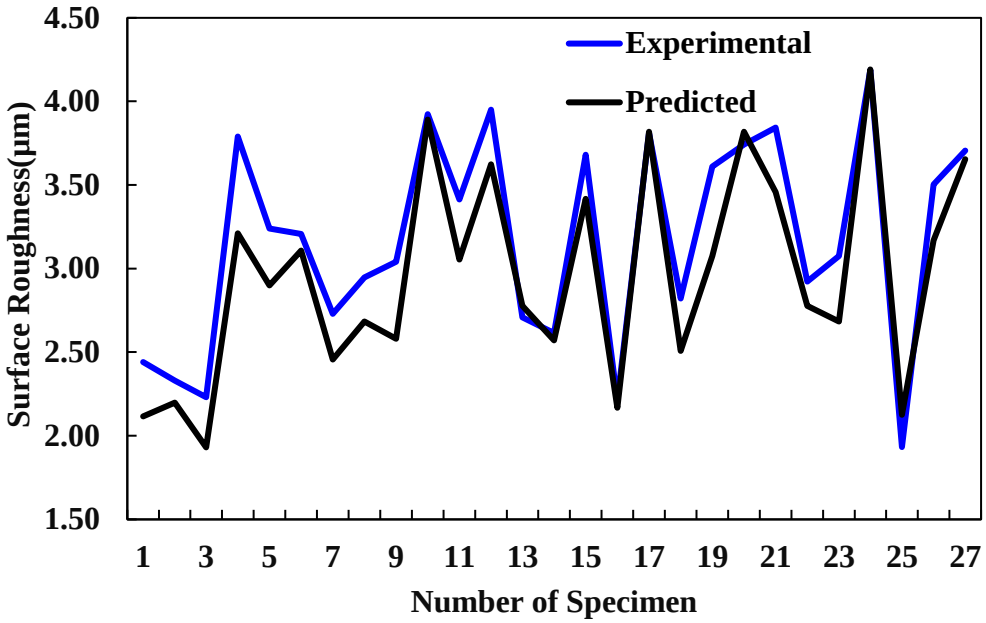

Figure 17 : Actual and predicted data for surface roughness model.

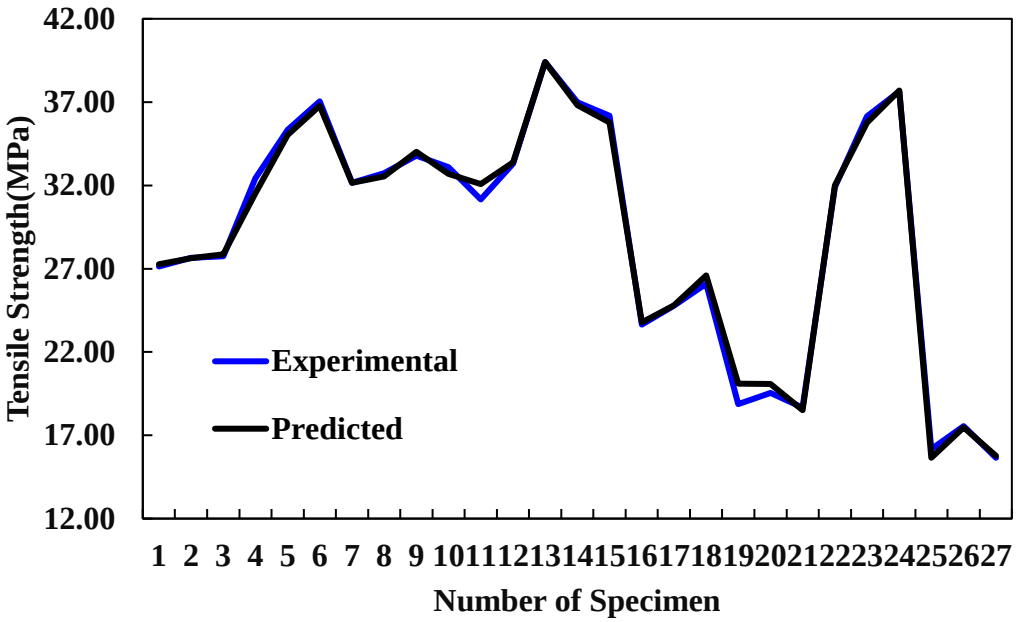

Figure 18 : Actual and predicted data for tensile strength model.

The root means square error analysis showed that the ANN model outperformed the combined model in predicting tensile strengths. As seen in Figure 18, the expected outcome was indistinguishable from the experimental findings, which increased the model's accuracy. The tensile strength model's root means square error (RMSE), which outperformed the combined prediction model, was determined to be 0.286078 for all data points. At epoch 4, the model's gradient was at its lowest point. At epoch 4, the smallest mean square error across training, validation, and testing data was identified, and the best validation performance was determined to be 0.46953. Additionally, it was discovered that the critical factor contributing to accurate prediction was the range of fluctuation of any output qualities. The RMSE values for the combined model and the normalized dataset's tensile strength model were very low, at 0.02028 (combined model) and 0.017766 (tensile strength model), respectively. Figure 19 explains how accurately the dimensional accuracy model predicted the experimental data.

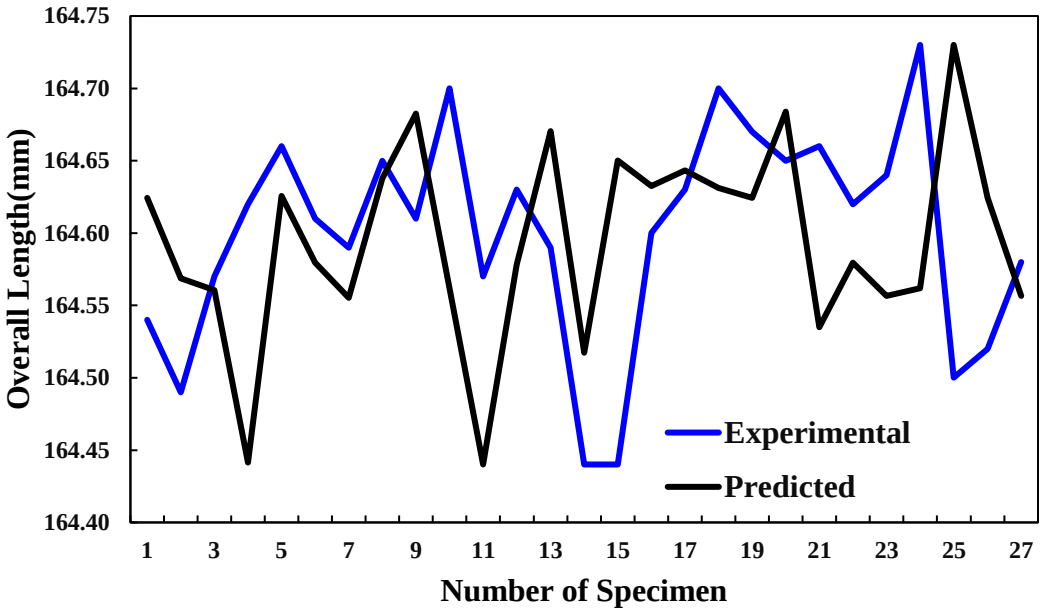
164.75
164.70
164.65
164.60
164.55
164.50
164.45
164.40
Overall Length(mm)
1
3
5
7
9
11
13
15
17
19
21
23
25
27
Number of Specimen
Experimental
Predicted

(a)

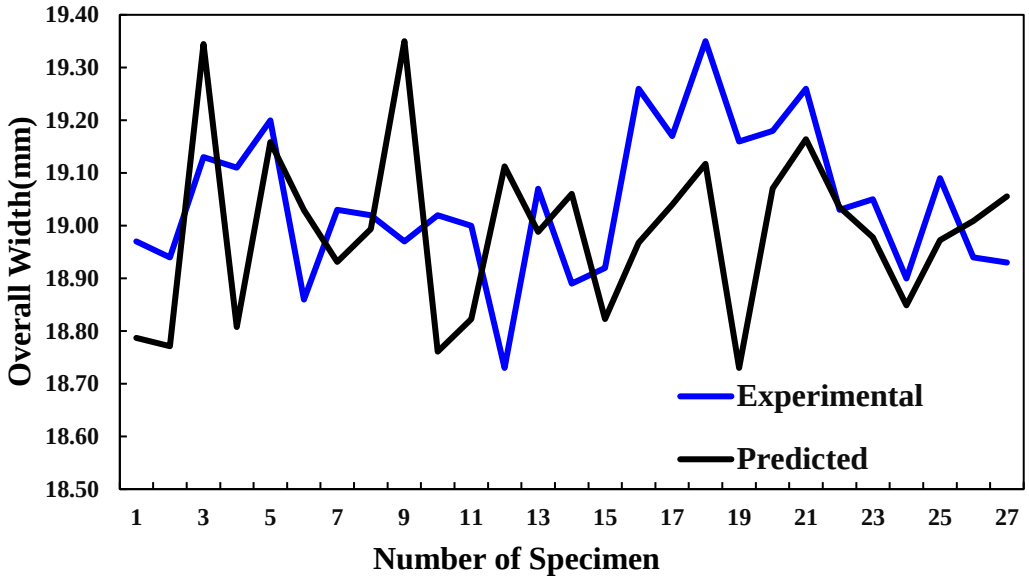
Overall Width(mm)
19.40
19.30
19.20
19.10
19.00
18.90
18.80
18.70
18.60
18.50
1
3
5
7
9
11
13
15
17
19
21
23
25
27
Number of Specimen
Experimental
Predicted

(b)

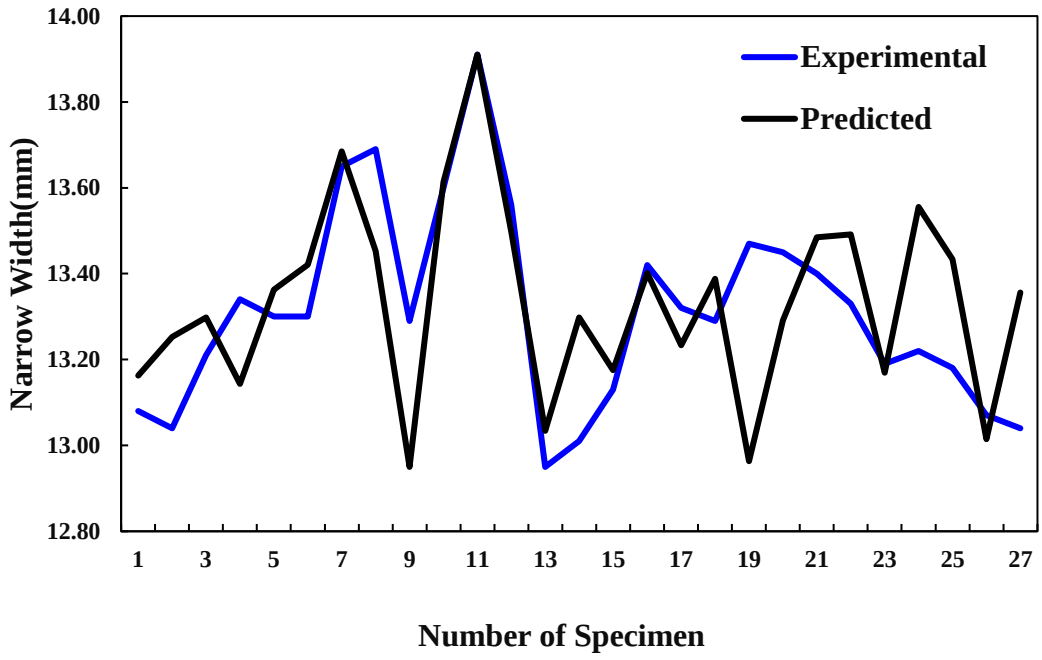
Narrow Width(mm)
14.00
13.80
13.60
13.40
13.20
13.00
12.80
1
3
5
7
9
11
13
15
17
19
21
23
25
27
Number of Specimen
Experimental
Predicted

(c)

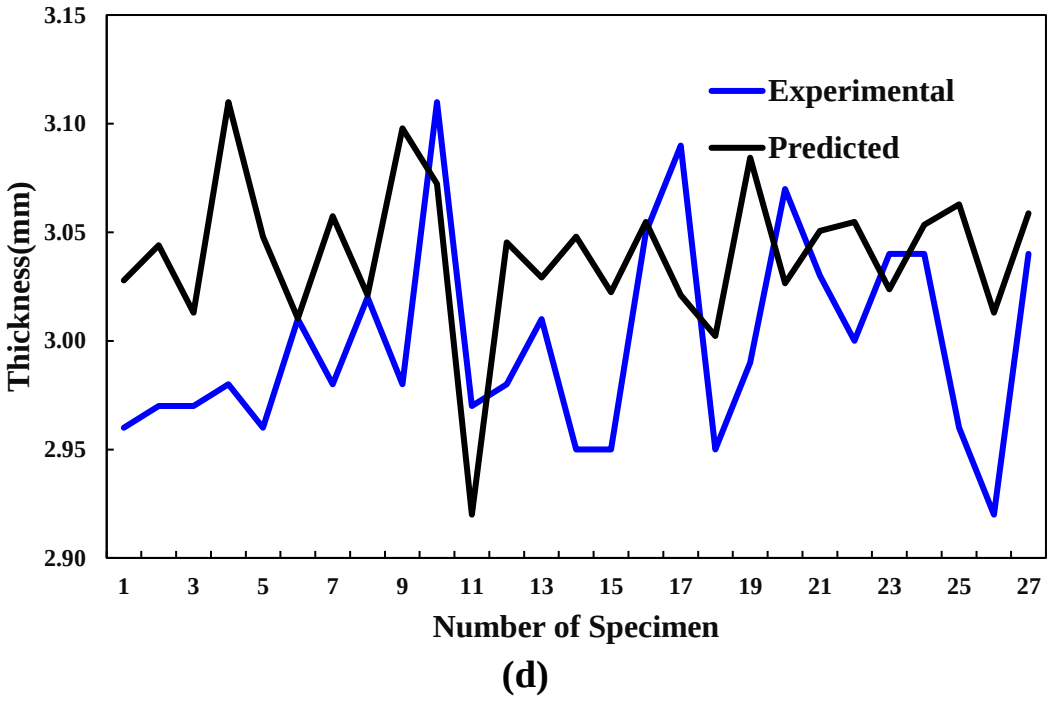

Figure 19 : Actual and predicted data for dimensional accuracy model: (a) overall length, (b) overall width, (c) narrow width, (d) thickness.

4.1.2 Effect of Process Parameters on Average Surface Roughness

According to Figure 21, the most critical process variables for determining the average surface roughness of the constructed specimen were layer thickness and deposition direction. The average surface roughness of the component was enhanced by increasing layer thickness and deposition direction. Low layer thickness and deposition direction supported the high surface finish level. The atoms' distribution in the bottom layer thickness and deposition direction was uniform. The interaction plot in Figure 20 demonstrated that for layer thicknesses of.2 and.3 mm, surface quality declined as the deposition direction increased from 30 to 45 degrees. The quality of the part's surface was less significantly impacted by extruder temperature. The product's

surface quality improved as the extruder's temperature rose. The nature of the atoms became more orderly and well-structured in each layer as the extruder's temperature climbed. As a result, surface roughness decreased as the extruder temperature increased. According to our analysis, surface roughness was most significant at a build orientation of 60 degrees. At a 60-degree build orientation, the support structure was mainly responsible for the most significant surface roughness. In a 90-degree construction orientation, the surface roughness marginally decreased. The build orientation with a zero-degree angle had the least surface roughness. The specimen's surface quality was less affected by printing speed, although slower printing produced a high-quality surface finish product.

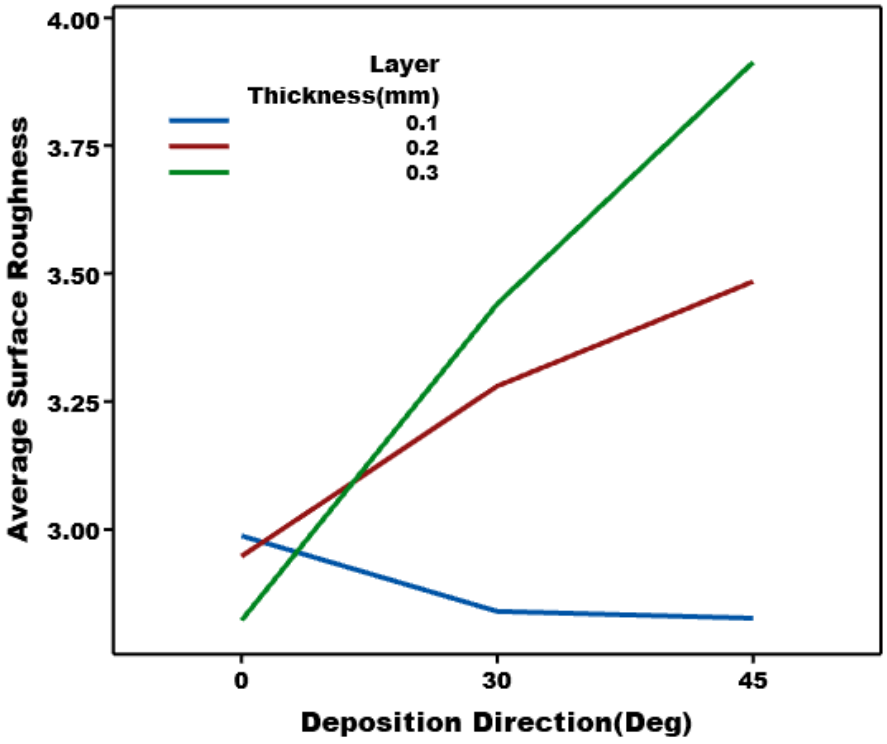

Figure 20 : Interaction plot between layer thickness and deposition direction for average surface roughness

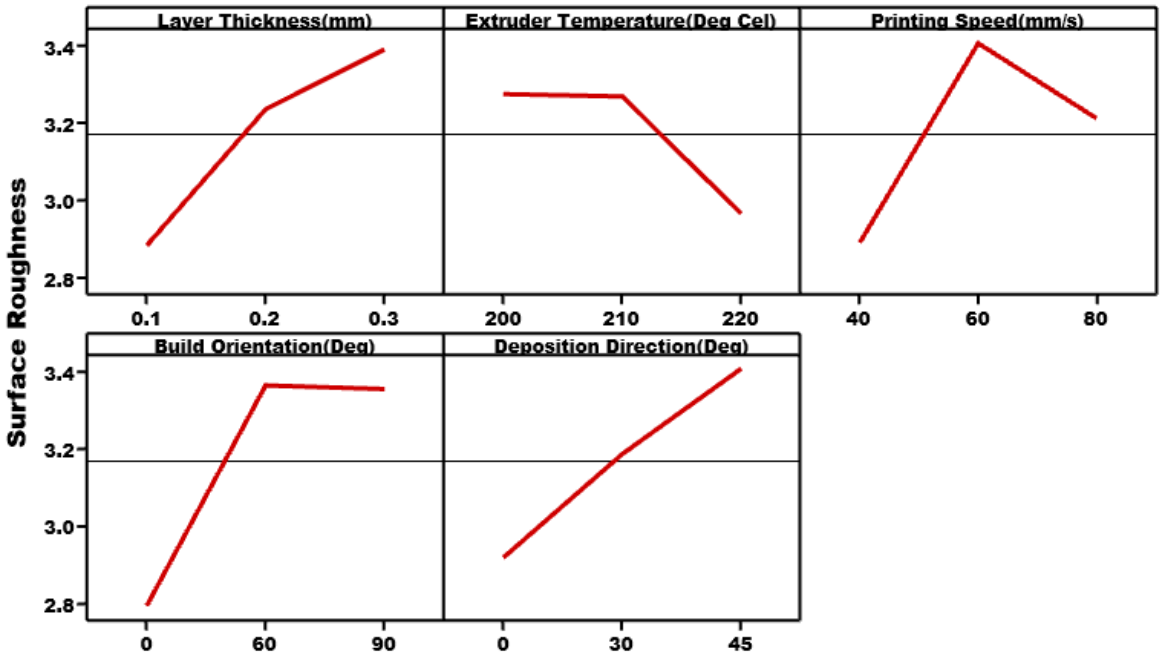

Figure 21 : Main effect plot of average surface roughness

4.1.3 Effect of Process Parameters on Tensile Strength

For enhancing the tensile strength of mechanical components, layer thickness, build orientation, and deposition direction (Figure 23) had the most significant effects. Although tensile strength increased with lower layer thickness but grew as build orientation and deposition direction increased. Lower layer thickness enhances interlayer adhesion and strengthens the part overall, whereas build orientation and deposition direction determine how the layers are oriented in reference to the applied force. Figure 22's interaction plot demonstrated that the maximum tensile strength was found in layers of .1mm thickness with 45-degree deposition directions. In contrast, the lowest tensile strength was found in layers of .3mm thickness with a 0-degree deposition direction. High extruder temperature makes strong atomic bonds which enhance the tensile strength of our constructed specimen. The strength of materials is marginally increased by faster printing; however, this influence is not as significant as that of other process variables. In

our research, we found that the maximum tensile strength of the materials is due mainly to the 210-degree extruder temperature of our specimen, with 200 and 220 degrees having a lesser effect on increasing tensile strength. At an extruder temperature of 210 degrees, the tensile strength was at its highest; extruder temperatures of 200 and 220 degrees had less of an impact. This is probably because the substance employed has a particular temperature range in which it demonstrates its optimum mechanical characteristics. Low temperatures may prevent the material from melting sufficiently, leading to poor layer adhesion and fragile sections. When temperatures rise over the ideal range, the material may melt excessively, leading to over-extrusion and a reduction in the part's strength. As a result, the material being utilized has reached its ideal temperature range of 210 degrees, enabling the finest possible combination of melting and flow qualities.

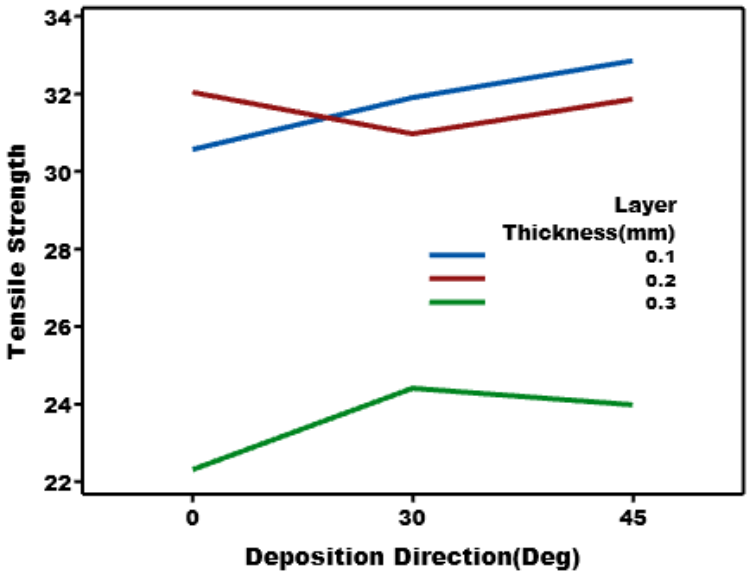

Figure 22 : Interaction plot between layer thickness and deposition direction for tensile strength

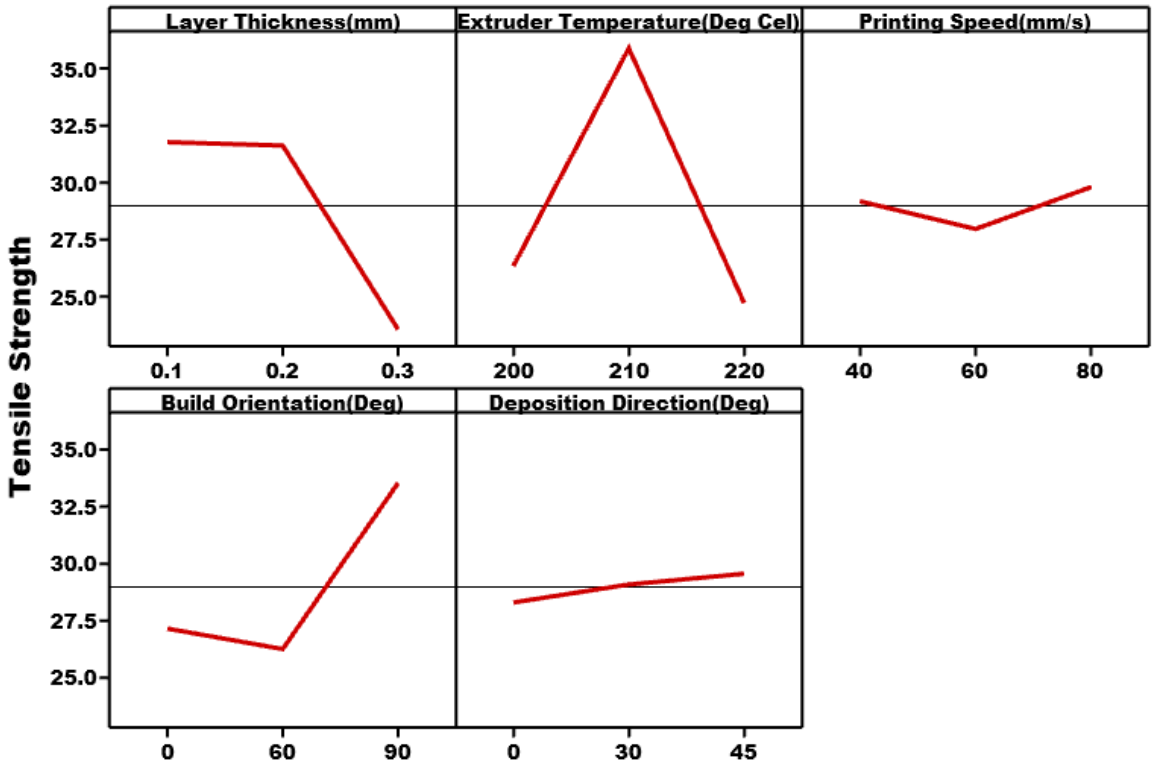

Figure 23 : Main effect plot of tensile strength

4.1.4 Effect of Process Parameters on Dimensional Accuracy

Although overall length accuracy declined as printing speed and extruder temperature rose, it increased with the layer thickness, deposition direction, and build orientation, as shown in Figure 24. The length accuracy of the printed part often decreases when extruder temperature and printing speed are raised. This is because rapid cooling and solidification from higher printing temperatures and rates can leave less time for the material to settle and connect with itself. This can result in dimensions that are off. The length accuracy of the printed part can be enhanced by increasing layer thickness, deposition direction, and construction orientation. Greater interlayer adhesion and less warping can be caused by thicker layer heights, which will produce more precise dimensions. Furthermore, printing in a specified deposition direction or

build orientation can reduce the effect of gravity or other external forces on the part during printing, leading to more precise dimensions.

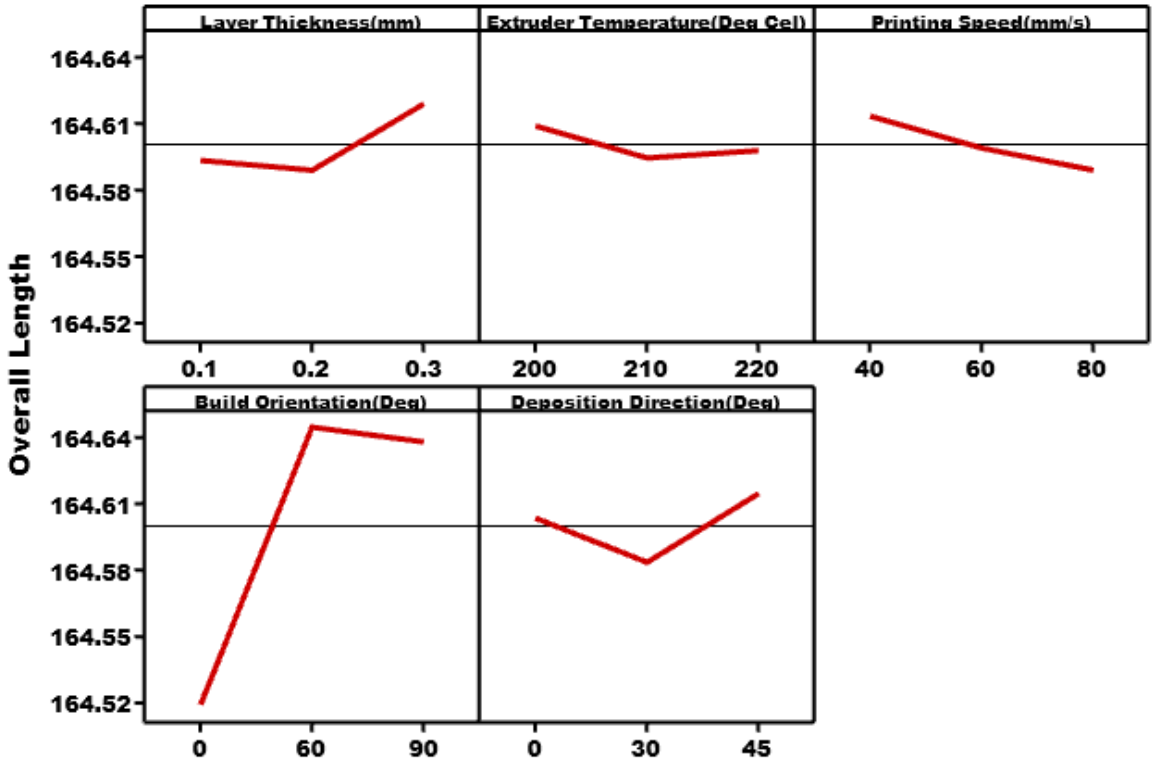

Figure 24 : Main effect plot of overall length

According to Figure 25, overall width accuracy increased with the increase in layer thickness, extruder temperature, and build orientation but fell with the decrease in deposition direction and printing speed. The precision of the printed part's width generally increases with layer thickness. The material deposition and adhesion between adjacent layers are improved by thicker layers. The improved interlayer adhesion keeps the printed part's desired width constant. Increased extruder temperatures also aid in improving width accuracy. An increase in extruder temperature makes the material more fluid and simpler to flow, which improves filling of the appropriate width. Greater material flow and deposition at higher temperatures aid in producing

dimensions that are more precise. By minimizing the effect of gravity on the printed object, specific building orientations lessen distortion. However, reducing the printing speed and deposition direction can have a negative impact on width accuracy. Overhanging or unsupported structures may result from lower deposition direction, which is the angle at which the material is deposited on the preceding layer. This could result in the printed part's width differing from its intended dimensions. Similar to this, faster printing rates may leave less time for each layer to adequately cool and solidify. Because of the limited cooling time, the material may twist or bend, giving the widths an incorrect reading. The ideal setting for precisely forecasting the final product's overall width was 0.1 mm layer thickness, 210°C extruder temperature, 60 mm/s printing speed, 0° build orientation, and 45° deposition direction.

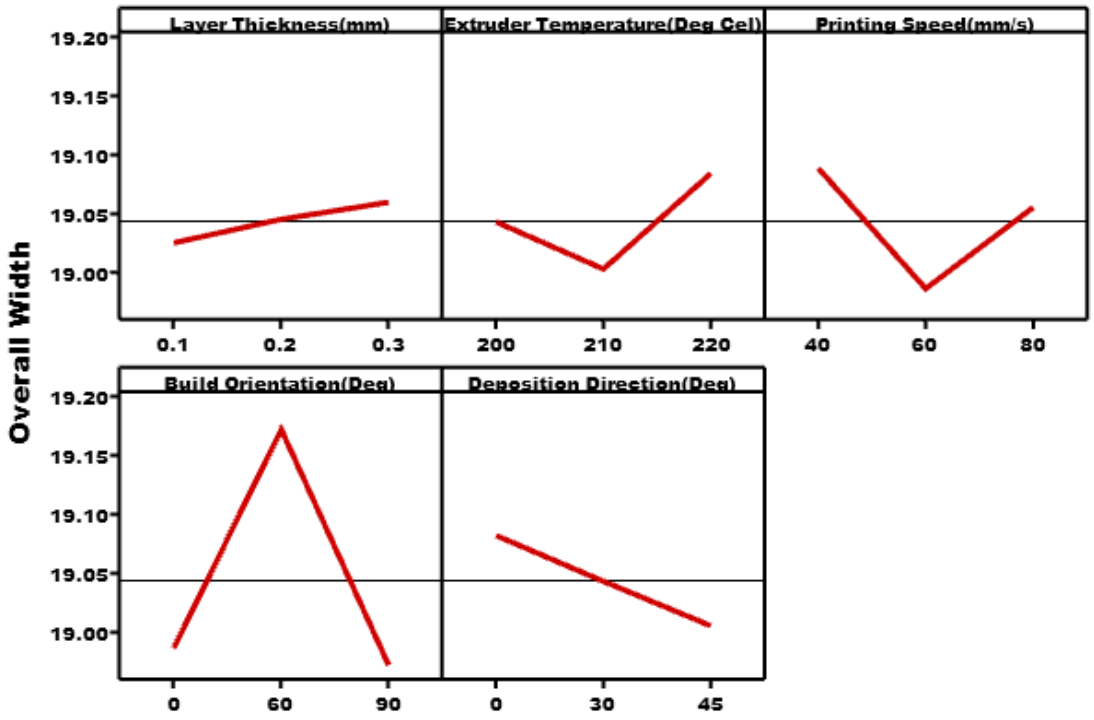

Figure 25 : Main effect plot of overall width

According to Figure 26, the ASTM standard specimen's narrow width accuracy increased when building orientation and printing speed decreased. The precision of the narrow width was also improved by increased layer thickness and deposition direction. The narrow width accuracy was less affected by extruder temperature, although 210 degrees produced the most remarkable results. Narrow width accuracy often increases when building orientation and printing speed decrease. This is a way to ensure the risk of distortion or warping of narrow features is diminished. Slower printing speeds and horizontal build orientations give the material more time to cool and solidify appropriately. As a result, narrow-width features may have more precise dimensions. Narrow-width accuracy can also be increased by increasing layer thickness and deposition orientation. More material per layer is provided by thick layers, which improve interlayer adhesion and bonding and allow for more precise dimensioning of features with narrow widths. To provide optimal support and adhesion for narrow features and further increase precision, consider the deposition direction, which is the angle at which the material is deposited on the preceding layer. The accuracy of narrow width is only marginally affected by extruder temperature. This is because printing speed and layer thickness, as opposed to extruder temperature, have a greater impact on material flow and deposition at narrow widths. To maintain optimal melting and flow qualities, it is still crucial to make sure the extruder temperature is within the acceptable range for the individual material being utilized.

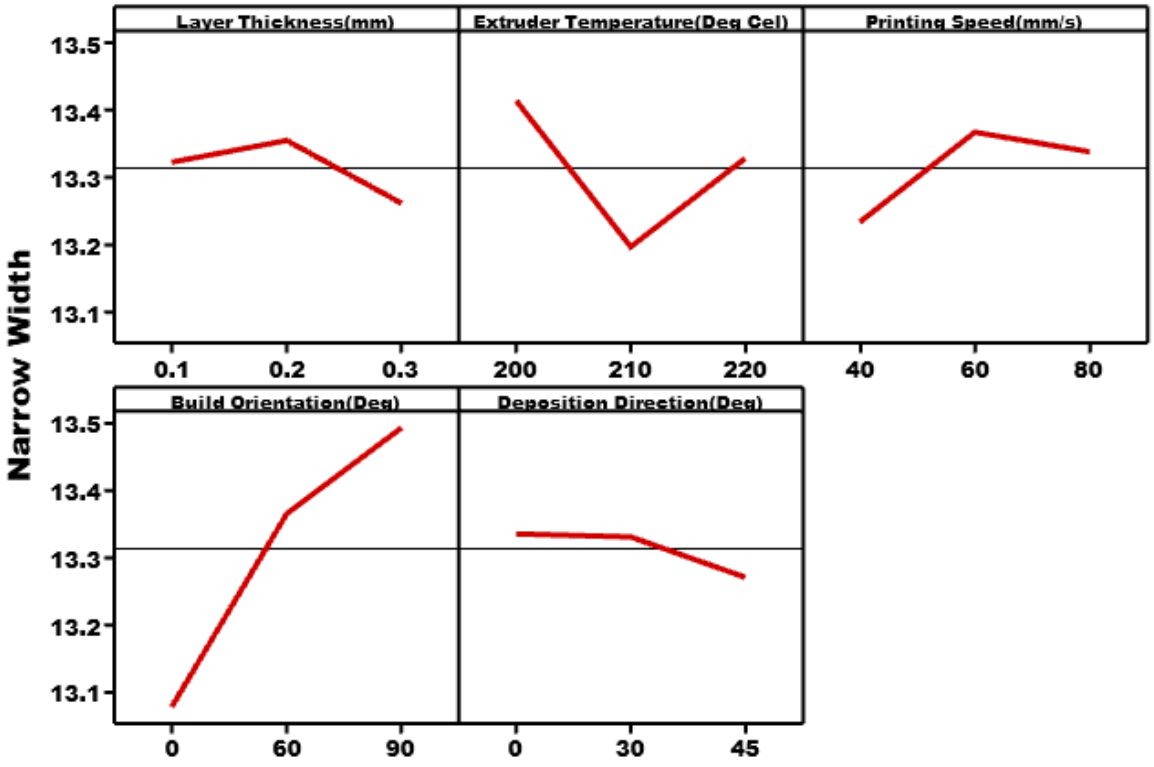

Figure 26 : Main effect plot of narrow width

The main effect plot demonstrated that the ideal parameters for accurately measuring the thickness of the produced specimen were 0.2 mm layer thickness, 220 °C extruder temperature, 80 mm/s printing speed, 60 ° build orientation, and 30 ° deposition direction. (Figure 27). A relatively thin layer thickness of 0.2 mm offers enough resolution to measure the thickness of the printed specimen. The material is adequately melted and extruded at a steady rate when the extruder is heated to a temperature of 220 °C, which is suitable for the material being utilized. With a printing speed of 80 mm/s, the specimen may be printed quickly and effectively without sacrificing the precision of the thickness measurement. The ideal build orientation is at a 60-degree angle since it lessens the distortion that might impair the precision of the thickness measurement by lessening the effect of gravity on the printed item. The adequate support and

adherence of the printed layers are ensured by the 30° deposition orientation, which might potentially affect the precision of the thickness measurement.

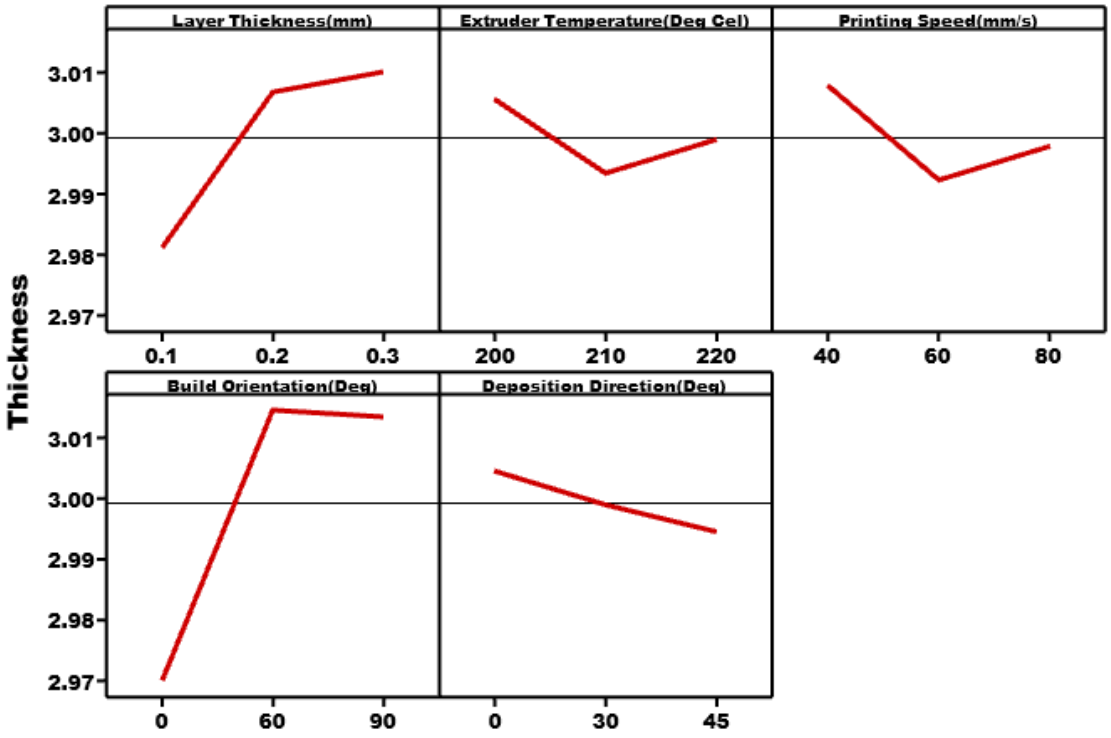

Figure 27 : Main effect plot of thickness

4.2 Results and Discussion for VLSTM modeling

4.2.1 VLSTM Modeling

In the second research, angular velocity vibration data of the printer bed was collected for specimens printed with four different combinations of printing speeds and deposition directions. The vibration data of specimen one was then used to train and test our developed VLSTM model. The model was trained using 70% of angular velocity data collected from the first four layers of the FDM printed parts and tested using the remaining 30% of angular velocity data collected from the fifth to sixth layers. Results showed that the testing dataset had excellent accuracy, particularly after training for an extended period.

It is essential to adjust the hyperparameters of any neural network based on the available dataset. All the adjusted parameters are listed in Table 7. One input layer, one hidden layer with four LSTM blocks, and one output layer demonstrated the time series dataset's significant machine angular velocity prediction capacity for producing FDM parts. After reshaping the input sample, the input layer of this network took a three-dimensional shape as input, where the first dimension represented the batch size, the second dimension meant the time step, and the third dimension represented the number of data used in the input sequence. To evaluate the pattern learning ability of our VLSTM network, we assessed the validation loss and root mean square error (RMSE). Our analysis indicates that the validation loss of our model is 0.0015, while the RMSE is found to be 0.062638, as shown in Table 6 (Specimen 1). These metrics serve as indicators of accuracy and suggest that the model can effectively learn and predict patterns in the data.

According to the findings of this study, the VLSTM model accurately predicts machine bed angular velocity based on the experimental data. Despite the high density of clustered data points, the model successfully replicated the patterns observed in the actual data. To illustrate the accuracy of the predictions, the predicted angular velocity data points for the last 100 test data are presented in Figure 28 (a). The experimental angular velocity data from Specimens 2, 3, and 4 were inserted in the developed model to check the time series prediction capabilities for different unknown printer speeds and deposition directions. Our developed model demonstrated excellent prediction results, as indicated by the lower RMSE value in Table 3s. The predicted test datasets are depicted in Figures 28 (b), (c), and (d). The time series data utilized for Specimens 2, 3, and 4 consisted of 800 data points. For specimens 2 and 4, training data was collected from the first three layers, and testing data was collected from the fourth layer.

However, for specimen 3, training data was collected from the first four layers, and testing data were collected from the fifth to sixth layers. as shown in Table 6.

Table 6 **:** Printing layer data used for training and testing along with RMSE results of all the dataset.

Specimen	Printing layers used for training	Printing layers used for testing	Total datasets used in LSTM network	RMSE
1	1-4	5-6	800	0.062638
2	1-3	4	800	0.039666
3	1-4	5-6	800	0.049107
4	1-3	4	800	0.034696

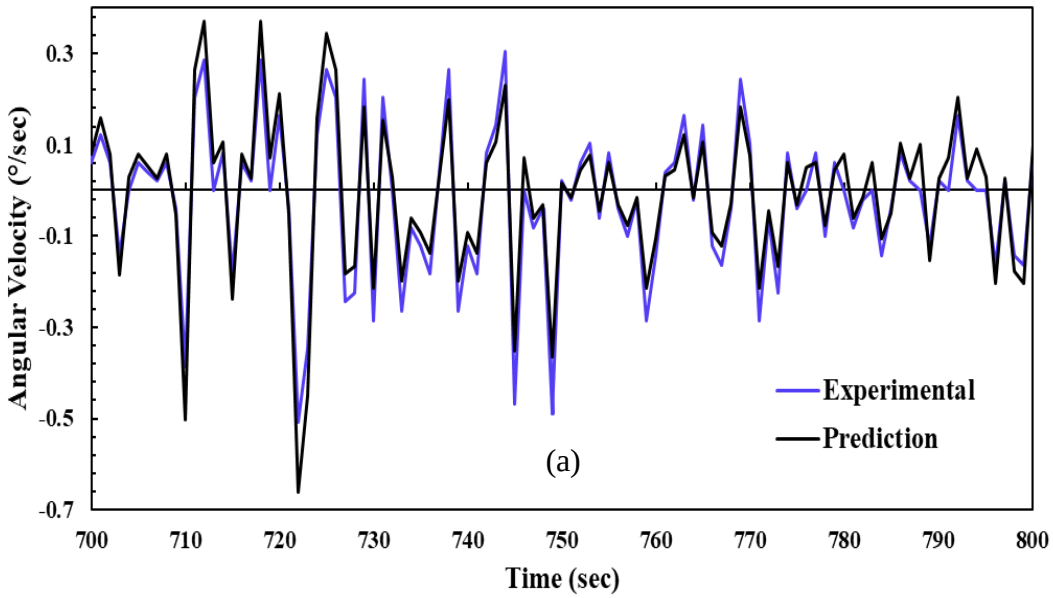

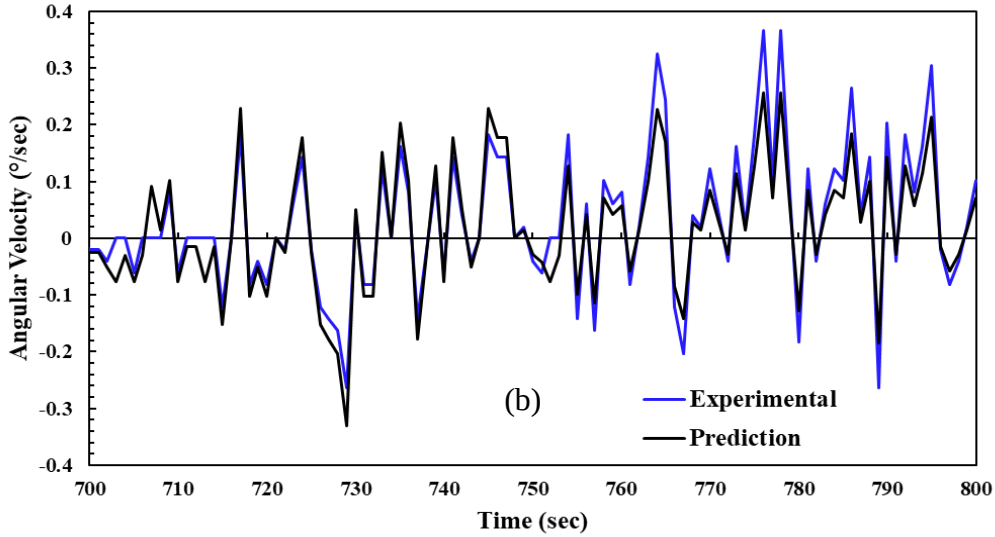
0.4
0.3
0.2
0.1
0
-0.1
-0.2
-0.3
-0.4
Angular Velocity (°/sec)
700
710
720
730
740
750
760
770
780
790
800
Time (sec)
(b)
Experimental
Prediction

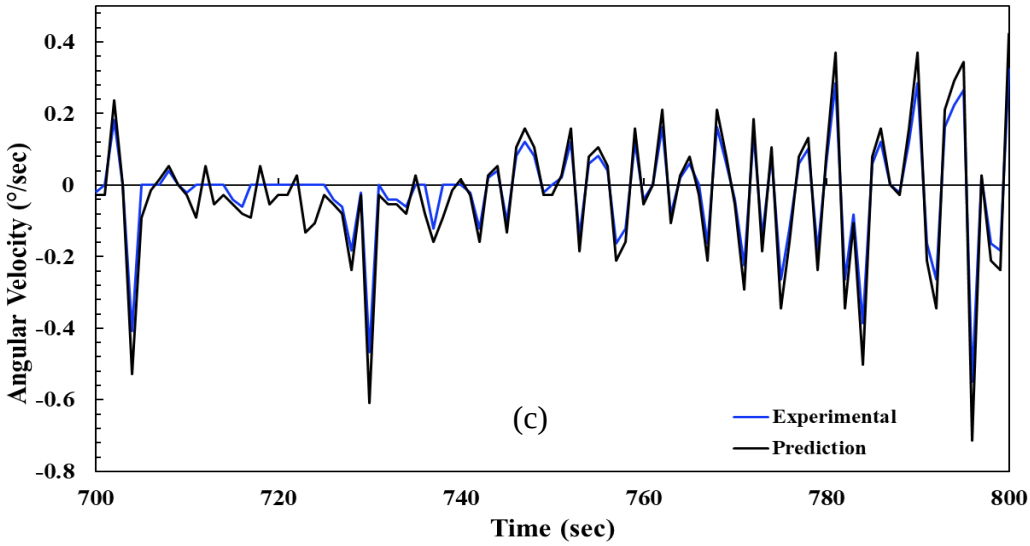
0.4
0.2
0
-0.2
-0.4
-0.6
-0.8
Angular Velocity (°/sec)
700
720
740
760
780
800
Time (sec)
(c)
Experimental
Prediction

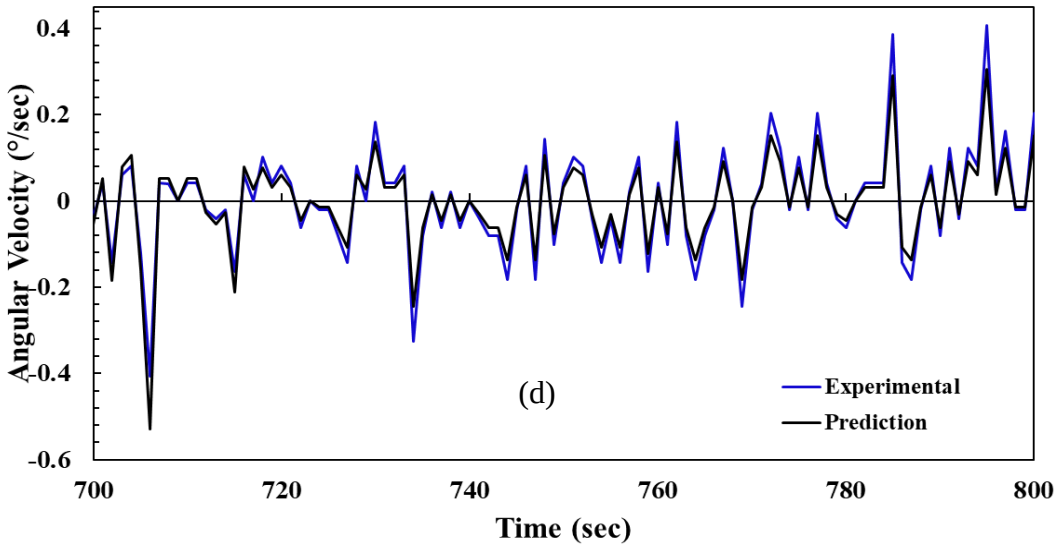

Figure 28 : Actual vs model predicted data for last 100 second test data for (a) specimen 1 (b) specimen 2 (c) specimen 3 (d) specimen 4.

Table 7 : Parameter setting for time series data prediction with VLSTM.

Hyperparameter	Value
Train to total data ratio	70%
Test to total data ration	30%
Optimizer	ADAM
Learning rate	0.001
Batch size	2
Number of epochs	100
Amount of total train data prediction	560
Amount of total test data prediction	240
Amount of total data	800
Data normalization range	0-1

4.2.2 Effect of Process Parameters on Printer Vibration

Based on the experimental investigation (Table 8), it was observed that maintaining a constant printing speed of 80 millimeters per second while changing the deposition direction from 45 to 0 degrees resulted in a higher average level of vibrations compared to maintaining a constant printing speed 40 millimeters per second. The main reason was that the nozzle had to change directions more frequently at the higher printer speed, which increased the printer bed's angular velocity (and thus the vibrations). On the other hand, the printer bed vibrated less when printing at a slower speed since the nozzle had more time to shift directions. When maintaining a constant deposition direction of 0 degrees and changing the printing speed from 40 to 80 degrees, it showed a higher average level of vibrations than maintaining a constant deposition direction of 45 degrees. The reason was that the nozzle head produced more kinetic energy as the nozzle head's velocity increased, which was then transmitted to the printer bed and finally resulted in higher levels of angular velocity. The nozzle head was going straight forward without changing direction if the deposition direction remained constant at 0 degrees. This resulted in the kinetic energy produced by the nozzle head being focused on a single path toward the printer bed, which can induce vibrations and even higher levels of angular velocity. Regarding specimen 2, a negative mean angular velocity indicated that the amplitude of the oscillations observed in the printer bed is more significant in the negative x, y, and z axes, relative to the positive x, y, and z axes. This could be caused by the uneven distribution of material weights in the printer bed.

Table 8 **:** Mean angular velocity of the specimen.

Specimen	Printing Speed (mm/sec)	Deposition Direction (deg)	Mean Angular Velocity (deg/sec)
1	80	45	0.00301
2	40	0	-0.00089
3	80	0	0.01030
4	40	45	0.00057

The interaction plot in Figure 29 showed that at 40 millimeters per second printing speed, when deposition direction increased from 0 to 45 degrees, mean angular velocity increased. So, the printer head must change directions more frequently when the deposition direction is changed from 0 to 45 degrees. This causes the printer head to generate more kinetic energy, which is then transferred to the printer bed and ultimately leads to higher vibrations. But, at 80 millimeters per second printing speed, data mean angular velocity decreased when deposition direction increased from 0 to 45. The printer head generated more kinetic energy at higher printing speeds, causing the printer bed to vibrate more. However, when the deposition direction was changed from 0 to 45 degrees, the printer head changed direction more frequently, which caused the kinetic energy to be distributed more evenly in different directions. This reduced the amplitude of vibrations because of the destructive nature of opposite kinetic energy in any single direction, resulting in a lower mean angular velocity. It was observed that the machine had a zero angular velocity in several printing layers when using a 0-degree deposition direction, which suggested that the machine was not experiencing any vibrations.

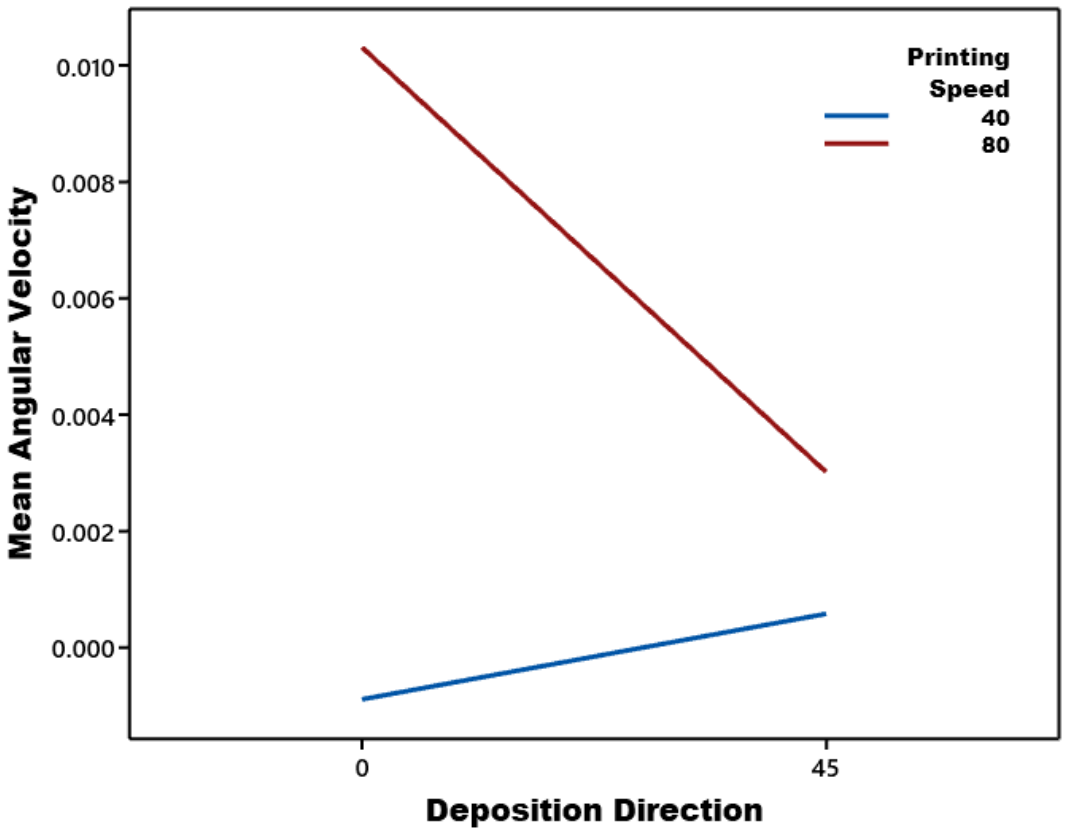

Figure 29 **:** Interaction plot between deposition direction and mean angular velocity making printing speed constant.

CHAPTER 5. CONCLUSIONS AND FUTURE WORKS

5.1 Conclusion and Future Work of First Study

The impact of layer thickness, extrusion temperature, printing speed, build direction, and deposition direction on the dimension accuracy, surface quality, and tensile strength of additively made components was examined in this study. Artificial neural network models were created using experimental data to depict the connection between these process factors and component properties. The training, validation, and testing outcomes for the proposed ANN models approximately match the experimental data, according to the root means square error (RMSE) analysis. Regarding the RMSE and correlation coefficient for the training, testing & validation data, the ANN models for the individual part characteristics outperformed the model for combining the three output part attributes.

We can summarize the following conclusions from our investigation:

a) The main effect plot result showed that to produce parts with superior surface quality, layer thickness, printing speed, build orientation, and deposition direction must be kept to a minimum. However, greater extruder temperatures produced pieces of exceptional quality. Therefore, the ideal combination of.1mm layer thickness, 220°C extruder temperature, 40 mm/s printing speed, 0° build orientation, and 0° deposition direction was found to make the best surface finish items.
b) Although the 210-degree extruder temperature of our manufactured specimen offered the best tensile strength, the main effect plot result revealed that increased printing speed, build orientation, and deposition direction created high tensile strength products. The

maximum tensile strength of materials was determined to be mostly due to decreased layer thickness. According to the results of our study, the mechanical characteristics of the produced specimen are improved by layer thicknesses.1 mm, 210℃ extruder temperatures, 80 mm/s printing speeds, 90° construction orientations, and 45° deposition directions.

c) The main effect plot findings showed that extruder temperature and deposition direction significantly influenced prototype parts' dimensional accuracy. Our research revealed that a 210° Celsius extruder temperature and a 45° deposition orientation were required to obtain the specimen's precise dimensions as a CAD model after fabricating an actual item. On the specimen's dimensional accuracy, layer thickness, printing speed, and build orientation had less of an impact.
d) It was discovered via RMSE that separate ANN models performed better than the combined model.

Future research should conduct further experiments to expand the size of the experimental dataset to enhance the accuracy of the ANN models because the practical dataset size in this study was constrained. Additionally, comparable predictive models may be used with various additive manufacturing processes.

5.2 Conclusion and Future Work of Second Study

The second study examined how process parameters of FDM technology affect the machine bed angular velocity based on time series data in FDM printing. A VLSTM neural network was developed to forecast the angular velocity data of future layers by using one combination of printing speed and deposition direction from a full factorial design. The model’s accuracy was

evaluated using RMSE, and the results indicated that predicted values closely matched the actual data. Moreover, testing the remaining printing speeds and deposition directions in the same model demonstrated the model's reliability and suitability for individual users.

The results of our investigation led to the following conclusions:

a) The analysis of RMSE results showed that A VLSTM network with one input layer, one hidden layer, and one output layer provided the most accurate prediction of machine bed angular velocity based on various unexplored infill patterns.

b) Interaction plots depicting the relationship between mean angular velocity and printer speed showed that as the printer speed increased, the mean angular velocity also increased.

c) For a deposition direction of 0 degrees, the angular velocity fluctuations remained zero for several layers after a certain period.

A limitation of this study was the significant simulation time required to tune the hyperparameters of the VLSTM network properly. Future research should focus on reducing this study's simulation time and using other new process parameters. Moreover, a similar model could be applied to time series temperature prediction in laser powder bed fusion technology.

REFERENCES

[1] N. Weake, M. Pant, A. Sheoran, and A. Haleem, "Optimising parameters of fused filament fabrication process to achieve optimum tensile strength using artificial neural network," 2020.

[2] R. Teharia, R. M. Singari, and H. Kumar, "Optimization of process variables for additive manufactured PLA based tensile specimen using taguchi design and artificial neural network (ANN) technique," *Mater. Today Proc.*, vol. 56, pp. 3426–3432, 2022.

[3] J. Femi-Oyetoro, "Prediction of mechanical properties of short fiber reinforced composite fabricated by Fused Filament Fabrication (FFF) method using Machine Learning," *Proc. Stud. Res. Creat. Inq. Day*, vol. 5, 2021.

[4] R. V. Pazhamannil, P. Govindan, and P. Sooraj, "Prediction of the tensile strength of polylactic acid fused deposition models using artificial neural network technique," *Mater. Today Proc.*, vol. 46, pp. 9187–9193, 2021.

[5] P. Charalampous, I. Kostavelis, T. Kontodina, and D. Tzovaras, "Learning-based error modeling in FDM 3D printing process," *Rapid Prototyp. J.*, vol. 27, no. 3, pp. 507–517, 2021.

[6] A. Pulipaka, K. M. Gide, A. Beheshti, and Z. S. Bagheri, "Effect of 3D printing process parameters on surface and mechanical properties of FFF-printed PEEK," *J. Manuf. Process.*, vol. 85, pp. 368–386, 2023.

[7] P. Wang, Y. Yang, and N. S. Moghaddam, "Process modeling in laser powder bed fusion towards defect detection and quality control via machine learning: The state-of-the-art and research challenges," *J. Manuf. Process.*, vol. 73, pp. 961–984, 2022.

[8] Md. S. R. Roney, N. Ahsan, H. Sezer, J. Tang, S. Kaul, and H. Ahmed, "Modeling Thermal Behavior and Residual Stress for Layer-by-Layer Rotated Scan Direction in Laser Powder Bed Fusion Process," in *IMECE2022*, Volume 2A: Advanced Manufacturing, Oct. 2022. doi: 10.1115/IMECE2022-95355.

[9] S. Ambruş, R. Muntean, C. Codrean, and I.-D. Uţu, "Influence of printing conditions on the mechanical properties of copper-polylactic acid composites obtained by 3d printing fused deposition modelling," *Mater. Today Proc.*, vol. 72, pp. 580–585, 2023.

[10] J. Deb, N. Ahsan, and S. Majumder, "Modeling the Interplay Between Process Parameters and Part Attributes in Additive Manufacturing Process With Artificial Neural Network," in *IMECE2022*, Volume 2A: Advanced Manufacturing, Oct. 2022. doi: 10.1115/IMECE2022-95120.

[11] O. A. Mohamed, S. H. Masood, and J. L. Bhowmik, "Modeling, analysis, and optimization of dimensional accuracy of FDM-fabricated parts using definitive screening design and deep learning feedforward artificial neural network," *Adv. Manuf.*, vol. 9, pp. 115–129, 2021.

[12] M. Shirmohammadi, S. J. Goushchi, and P. M. Keshtiban, "Optimization of 3D printing process parameters to minimize surface roughness with hybrid artificial neural network model and particle swarm algorithm," *Prog. Addit. Manuf.*, vol. 6, pp. 199–215, 2021.

[13] M. Goudswaard, B. Hicks, and A. Nassehi, "The creation of a neural network based capability profile to enable generative design and the manufacture of functional FDM parts," *Int. J. Adv. Manuf. Technol.*, vol. 113, pp. 2951–2968, 2021.

[14] M. A. Ablat, H. Abedi, and A. Qattawi, “Modeling the influence of fused filament fabrication processing parameters on the mechanical properties of ABS parts,” *J. Manuf. Process.*, vol. 71, pp. 711–723, 2021.
[15] A. N. Ahsan, M. A. Habib, and B. Khoda, “Resource based process planning for additive manufacturing,” *Comput.-Aided Des.*, vol. 69, pp. 112–125, 2015.
[16] N. Ahsan and B. Khoda, “AM optimization framework for part and process attributes through geometric analysis,” *Addit. Manuf.*, vol. 11, pp. 85–96, 2016.
[17] X. Qi, G. Chen, Y. Li, X. Cheng, and C. Li, “Applying neural-network-based machine learning to additive manufacturing: current applications, challenges, and future perspectives,” *Engineering*, vol. 5, no. 4, pp. 721–729, 2019.
[18] J. F. Arinez, Q. Chang, R. X. Gao, C. Xu, and J. Zhang, “Artificial intelligence in advanced manufacturing: Current status and future outlook,” *J. Manuf. Sci. Eng.*, vol. 142, no. 11, 2020.
[19] A. Tura, H. Mamo, Y. Jelila, and H. Lemu, “Experimental investigation and ANN prediction for part quality improvement of fused deposition modeling parts,” presented at the IOP Conference Series: Materials Science and Engineering, IOP Publishing, 2021, p. 012031.
[20] D. Chhabra and R. Gupta, “Optimization of FDM printing parameters for surface quality improvement of carbon based nylon (PA-CF) composite material fabricated parts using evolutionary algorithm,” *J. Nano- Electron. Phys.*, vol. 13, no. 2, 2021.
[21] K. Kandananond, “Surface roughness prediction of FFF-fabricated workpieces by artificial neural network and Box–Behnken method,” *Int. J. Metrol. Qual. Eng.*, vol. 12, p. 17, 2021.
[22] S. K. Everton, M. Hirsch, P. Stravroulakis, R. K. Leach, and A. T. Clare, “Review of in-situ process monitoring and in-situ metrology for metal additive manufacturing,” *Mater. Des.*, vol. 95, pp. 431–445, 2016.
[23] E. W. Reutzel and A. R. Nassar, “A survey of sensing and control systems for machine and process monitoring of directed-energy, metal-based additive manufacturing,” *Rapid Prototyp. J.*, vol. 21, no. 2, pp. 159–167, 2015.
[24] G. Tapia and A. Elwany, “A review on process monitoring and control in metal-based additive manufacturing,” *J. Manuf. Sci. Eng.*, vol. 136, no. 6, 2014.
[25] W. E. Frazier, “Metal additive manufacturing: a review,” *J. Mater. Eng. Perform.*, vol. 23, pp. 1917–1928, 2014.
[26] P. K. Rao, J. Liu, D. Roberson, Z. Kong, and C. Williams, “Online real-time quality monitoring in additive manufacturing processes using heterogeneous sensors,” *J. Manuf. Sci. Eng.*, vol. 137, no. 6, p. 061007, 2015.
[27] K. Menderes, H. Saruhan, and A. Ipekci, “Investigation the effects of 3D printer system vibrations on mechanical properties of the printed products,” *Sigma J. Eng. Nat. Sci.*, vol. 36, no. 3, pp. 655–666, 2018.
[28] J. B. Deb, A. Paul, and S. Barman, “Aerodynamics of Airfoil Upon Introduction of a Circular Rotary Trailing Edge”.
[29] M. A. I. Yousuf, N. A. M. J. B. Deb, and M. H. Bappy, “A Research Framework of Supply Chain Logistics using Horizontal Collaboration for Developing Countries,” presented at the MESSAGE FROM THE CONFERENCE CHAIRS, p. 167.
[30] S. A. Ratna, F. Rahman, M. A. I. Yousuf, and J. B. Deb, “An Explanatory Study of the Present Scenario of Credit Risk Management in the Banking Sector,” presented at the MESSAGE FROM THE CONFERENCE CHAIRS, p. 177.

[31] J. Giri, P. Shahane, S. Jachak, R. Chadge, and P. Giri, “Optimization of FDM process parameters for dual extruder 3d printer using Artificial Neural network,” *Mater. Today Proc.*, vol. 43, pp. 3242–3249, 2021.
[32] S. Hochreiter and J. Schmidhuber, “Long short-term memory,” *Neural Comput.*, vol. 9, no. 8, pp. 1735–1780, 1997.
[33] J. Zhang, Y. Zeng, and B. Starly, “Recurrent neural networks with long term temporal dependencies in machine tool wear diagnosis and prognosis,” *SN Appl. Sci.*, vol. 3, pp. 1–13, 2021.
[34] A. Sherstinsky, “Fundamentals of Recurrent Neural Network (RNN) and Long Short-Term Memory (LSTM) Network. eprint,” *ArXiv Prepr. ArXiv180803314*, 2018.
[35] X.-Y. Li, F.-L. Liu, M.-N. Zhang, M.-X. Zhou, C. Wu, and X. Zhang, “A Combination of Vision-and Sensor-Based Defect Classifications in Extrusion-Based Additive Manufacturing,” *J. Sens.*, vol. 2023, 2023.
[36] M. Hikmat, S. Rostam, and Y. M. Ahmed, “Investigation of tensile property-based Taguchi method of PLA parts fabricated by FDM 3D printing technology,” *Results Eng.*, vol. 11, p. 100264, 2021.
[37] S. Negi, S. Dhiman, and R. K. Sharma, “Basics and applications of rapid prototyping medical models,” *Rapid Prototyp. J.*, vol. 20, no. 3, pp. 256–267, 2014.
[38] N. Kumar, P. K. Jain, P. Tandon, and P. M. Pandey, “The effect of process parameters on tensile behavior of 3D printed flexible parts of ethylene vinyl acetate (EVA),” *J. Manuf. Process.*, vol. 35, pp. 317–326, 2018.
[39] H. P. Nagarajan *et al.*, “Knowledge-based design of artificial neural network topology for additive manufacturing process modeling: a new approach and case study for fused deposition modeling,” *J. Mech. Des.*, vol. 141, no. 2, p. 021705, 2019.
[40] G. A. Adam and D. Zimmer, “Design for Additive Manufacturing—Element transitions and aggregated structures,” *CIRP J. Manuf. Sci. Technol.*, vol. 7, no. 1, pp. 20–28, 2014.
[41] R. Hague, S. Mansour, and N. Saleh, “Design opportunities with rapid manufacturing,” *Assem. Autom.*, vol. 23, no. 4, pp. 346–356, 2003.
[42] F. S. Panchal and M. Panchal, “Review on methods of selecting number of hidden nodes in artificial neural network,” *Int. J. Comput. Sci. Mob. Comput.*, vol. 3, no. 11, pp. 455–464, 2014.
[43] M. Zakaulla and S. kesarmadu Siddalingappa, “Prediction of mechanical properties for polyetheretherketone composite reinforced with graphene and titanium powder using artificial neural network,” *Mater. Today Proc.*, vol. 49, pp. 1268–1274, 2022.
[44] S. T. Alexander and S. T. Alexander, “The Mean Square Error (MSE) Performance Criteria,” *Adapt. Signal Process. Theory Appl.*, pp. 8–33, 1986.
[45] T. Chai and R. R. Draxler, “Root mean square error (RMSE) or mean absolute error (MAE),” *Geosci. Model Dev. Discuss.*, vol. 7, no. 1, pp. 1525–1534, 2014.
[46] P. Srisaeng, G. S. Baxter, and G. Wild, “Forecasting demand for low-cost carriers in Australia using an artificial neural network approach,” *Aviation*, vol. 19, no. 2, pp. 90–103, 2015.
[47] Y. Hu, A. Huber, J. Anumula, and S.-C. Liu, “Overcoming the vanishing gradient problem in plain recurrent networks,” *ArXiv Prepr. ArXiv180106105*, 2018.
[48] S. Squartini, A. Hussain, and F. Piazza, “Preprocessing based solution for the vanishing gradient problem in recurrent neural networks,” presented at the Proceedings of the 2003 International Symposium on Circuits and Systems, 2003. ISCAS’03., IEEE, 2003, p. V–V.